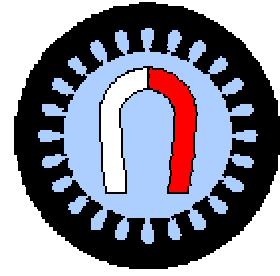




**KUNGL
TEKNISKA
HÖGSKOLAN**

Permanent
Magnet
Drives



Theoretical design of surface-mounted permanent magnet motors with field- weakening capability

by

Stephan Meier

Master Thesis

**Supervisors:
Dr. Juliette Soulard
Robert Chin**

Royal Institute of Technology
Department of Electrical Engineering
Electrical Machines and Power Electronics

Stockholm 2001/2002

Theoretical design of surface-mounted permanent magnet motors with field-weakening capability

Abstract

This master thesis deals with the design of an permanent magnet (PM) motor for electric vehicles. An analytical model for surface mounted PM-motors (SMPM) is derived and verified with finite element analysis (FEM). Special attention is paid to the iron losses as they influence the performances.

Today's motors for traction in electric vehicles are most often induction motors. In recent years, PM-motors have become interesting, as the efficiency can be increased. This is very important in battery applications.

The first part of the project consisted of a literature study that aimed at building knowledge on machine design for field weakening applications. An analytical model for SPM-motors was deduced thereupon.

An analytical model for the design of SMPM-motors was implemented in Matlab. It was verified with two-dimensional FEM calculations (Flux2D). It was noticed, that an optimal analytical design tool requires good means for predicting the iron losses. This is due to the fact that the iron losses form a significant fraction of the total losses in SMPM-motors and therefore have a big influence on the performances.

Based on the results from the FEM analysis, an iron loss model for the stator teeth and the stator yoke was derived. This iron loss model is based on the description of the flux created by the magnets and the currents in the respective areas. The influence of the stator leakage is included as well. The iron loss model covers the complete operational range. An improved model attempting to include the leakage flux was also derived.

Based on the computer program, some designs and the influence of certain parameters as the number of poles or the airgap length are discussed. The design that uses the stator of the induction motor that shall be replaced is of special interest. In addition, a compact design is presented.

Keywords

Surface-Mounted PM-motor (SMPM), Field-Weakening, Electric Vehicles, Iron Loss Model, Flux Distribution, Stator Leakage.

Acknowledgement

This master thesis was written at the Department of Electrical Engineering, Division of Electrical Machines and Power Electronics, Royal Institute of Technology (KTH), Stockholm. The work was part of the Permanent Magnet Drives Program (PMD) at the Competence Centre in Electric Power Engineering. It lasted for four months in the period from October 2001 to March 2002.

This master thesis was supported by the Department of Information Technology and Electrical Engineering, Division of Electrical Engineering and Design Laboratory, Swiss Federal Institute of Technology (ETH), Zurich. I would like to thank Prof. Jörg Hugel for the supervision of my diploma work in Switzerland.

A special thank goes to Prof. Chandur Sadarangani for enabling me to write this master thesis in Stockholm at his department.

I am very grateful to my supervisor Dr. Juliette Soulard and to Robert Chin for excellent assistance during my whole work.

I would like to say thanks to the staff of the whole department for supporting and helping me in any way. I will never forget the good time I had at your department, including the Roebel's bar, the Surströming, the Santa Lucia Christmas party, the innebandy games etc.

For the support in administrative matters I would like to thank the secretary of the Department of Information Technology and Electrical Engineering, Mr. M. Kreuzer and all involved persons from the student exchange offices in Zurich and Stockholm.

Finally I would like to thank all my friends and especially my family for the financial and moral support during my studies.

A handwritten signature in black ink that reads "S. Meier". The letters are cursive and slightly slanted to the right.

Stephan Meier
A snowy day in Stockholm,
March 2002

Contents

1 Introduction	1
2 Literature review on field-weakening operation	2
2.1 Principal of field-weakening operation	2
2.2 Synchronous AC motors.....	4
2.2.1 Coherence between different field-weakening motors.....	4
2.2.2 Main classes of synchronous AC motors	5
2.2.3 IPM parameter plane	6
2.3 Field-weakening operation of Permanent Magnet Motors.....	7
2.3.1 Optimal field-weakening operation.....	9
2.4 Practical limitations and factors	10
3 The SMPM drive	12
3.1 Normalisation	12
3.1.1 Operation at rated speed	13
3.2 Maximum torque field-weakening control.....	14
3.3 SMPM characteristics.....	16
4 Analytical Design.....	17
4.1 Design process.....	18
4.1.1 Magnetic design.....	21
4.1.2 Operation performance	22
4.1.3 Loss models	26
4.1.4 Armature reaction and magnet protection	31
4.2 Parameter study	33
4.2.1 Dimensions of the basic geometry	33
4.2.2 Influence of the number of poles.....	35
4.2.3 Compact design	36
4.2.4 Variations on the rotor geometry.....	38
5 Verification with FEM	40
5.1 Setup of the Flux2D-Simulation.....	40
5.1.1 Constructing the geometry and the mesh	40
5.1.2 Description of the materials.....	41
5.1.3 Electrical circuits and description of the physical properties.....	43
5.1.4 Solving processor	45
5.2 Results	45
5.2.1 No-load simulation	45
5.2.2 Operation at rated speed	47

5.2.3 Field-weakening operation	50
5.3 Improved analytical iron loss model	53
5.3.1 Losses in the stator teeth.....	53
5.3.2 Stator yoke losses	55
5.3.3 Leakage model.....	58
6 Conclusions and future work	63
App. A Powder materials and concentrated windings.....	68
App. B Parameter calculations	69
App. B1 Calculation of the magnetising inductances	69
App. B2 Calculation of the stator leakage inductance	70
App. B3 Calculation of the scaling factor for the radial yoke flux component.....	72
App. C Park transformation	73
App. D Magnet shape and magnetisation	74

1 Introduction

Today's motor for traction in electric vehicles is most often an induction motor. For some applications the characteristic of the induction motor, especially the field weakening range, fits the application demands very well. However, the efficiency is very important in these battery applications and therefore a system with a permanent magnet motor is promising.

The goal of this master thesis is to design a surface mounted permanent magnet motor (SMPM) for field-weakening operation. Based on analytical models and finite element analysis, the possibilities and limitations of the SMPM are investigated.

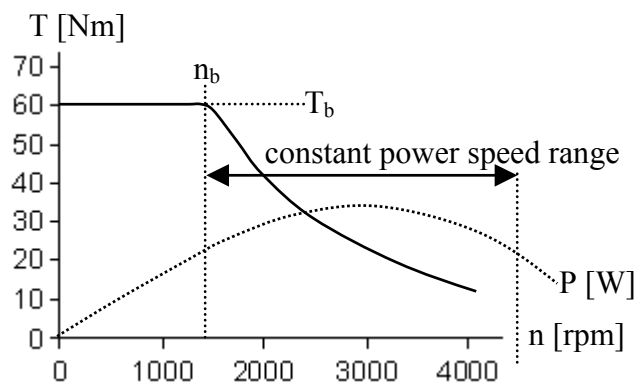


Figure 1-1 Torque versus speed characteristic for the forklift

Figure 1-1 shows the required torque versus speed characteristic for the application in a forklift. The idea is to design a SPM motor so that the drive gets the performance like the one presented in Figure 1-1. The nominal torque T_b is 60 Nm and the nominal speed n_b is 1500 rpm. The nominal power P_b is 9.42 kW. The maximum speed at constant power is 4500 rpm. This implies a constant power range of 3.

2 Literature review on field-weakening operation

In this chapter, the field-weakening operation is introduced. The principal of field-weakening operation is exemplified by the separately excited DC commutator motor drive, which shows an ideal field-weakening characteristic. Thereafter the main types of brushless synchronous AC motors are introduced and their coherence to the separately excited DC commutator motor drive is outlined. In section 2.3 the field-weakening operation of permanent magnet motors in general is investigated. The chapter closes with some comments on practical aspects and limitations.

2.1 Principal of field-weakening operation

The separately excited DC commutator motor drive shows an ideal field-weakening characteristic. Therefore it is appropriate to consider the principal of field-weakening operation using this familiar motor characteristic.

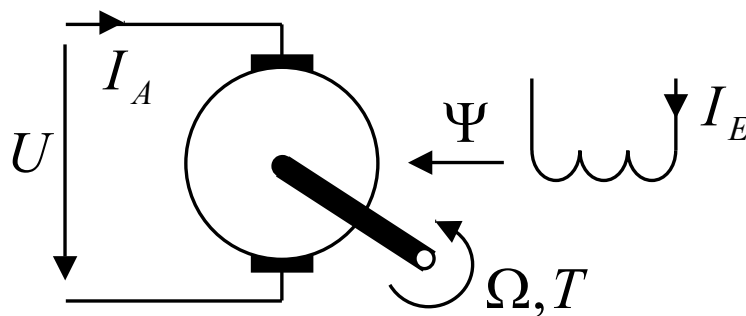


Figure 2-1 Separately excited DC commutator motor drive

In this drive the excitation flux Ψ is controlled by the DC field-current I_E . The torque T is the product of the armature current I_A and the flux Ψ , and the induced voltage U is the product of the angular frequency (or electrical speed) Ω and the flux Ψ (see Figure 2-1 for a simplified charting of the separately excited DC commutator motor drive, armature and excitation resistance as well as armature inductance are neglected).

$$\Psi = k_{\Psi} \cdot I_E \quad \text{Equation 2-1}$$

$$T = I_A \cdot \Psi \quad \text{Equation 2-2}$$

$$U = \Omega \cdot \Psi \quad \text{Equation 2-3}$$

At low speed, the rated armature current I_{Ab} and the rated excitation-flux Ψ_b are used to obtain the rated torque T_b . The voltage U and output power P_{out} both rise linearly with speed. This operating range is referred to as constant-torque or constant-flux region. At rated speed n_b , the voltage equals the rated voltage U_b (the maximum voltage available). Above rated speed, the voltage is kept constant and the flux is decreased (weakened).

The torque is inversely proportional to the speed increase. As the power is constant beyond the rated speed ($P_{out} = P_b$), this is called constant-power region or field-weakening region. These terms are normally used interchangeably in literatures though one should be careful with the latter as it is usually possible to keep increasing the speed at a reduced power.

Figure 2-2 shows the ideal field-weakening characteristics for a drive with a limited inverter volt-ampere rating capability.

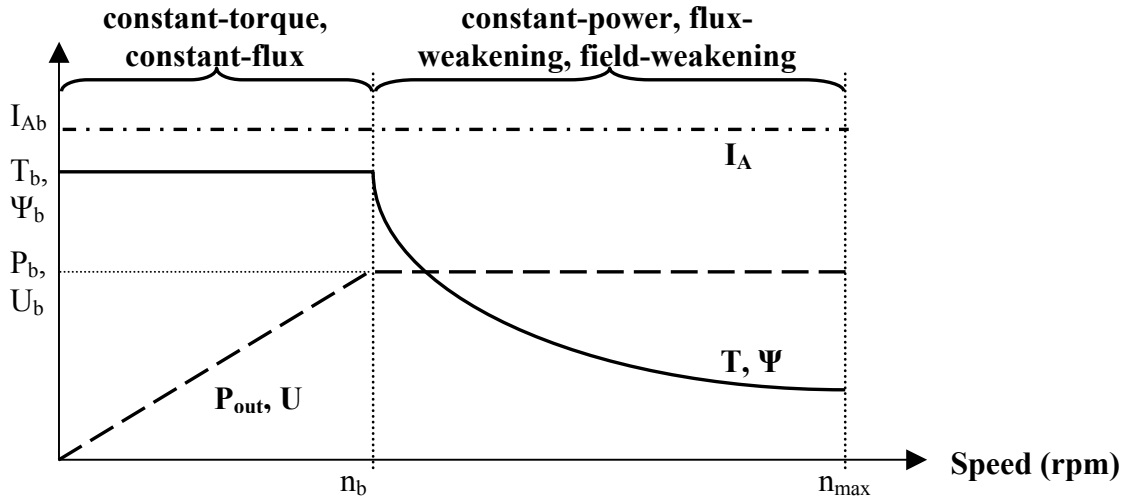


Figure 2-2 Ideal field-weakening drive characteristics

Real motors do not have flat output power against speed characteristics above rated speed n_b . In Figure 2-1 the dashed line is the ideal field-weakening characteristic and the solid line is the actual characteristic. Rated power is the output power at rated speed n_b with rated torque T_b . The inverter utilisation is the ratio of rated power to the ideal output power. This is less than unity as the motor does not have unity power factor and 100% efficiency under rated operating conditions. The constant-power speed range (CPSR) is the speed range over which rated power can be maintained.

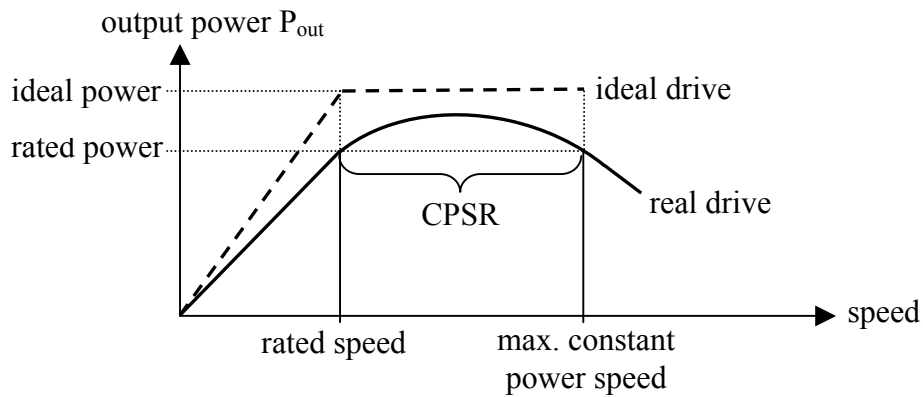


Figure 2-3 Definition of field-weakening parameters

2.2 Synchronous AC motors

In this section, the coherence between the separately excited DC commutator motor drive and the synchronous AC permanent magnet motor is outlined. Then, to prepare for the introduction in field-weakening operation of permanent magnet motors in section 2.3, an introduction to the main types of synchronous AC motors is given. Their possible field-weakening performance is graphically shown on the IPM parameter plane [1].

2.2.1 Coherence between different field-weakening motors

This section is an addition to outline the coherence between different motors with field-weakening capabilities. The differences and similarities of several motor principles are outlined and the choice of their names in this master thesis is explained. In the literature you can find various names for the same motor, based on different approaches or points of view. Figure 2-4 shows the cross-section of three different motors.

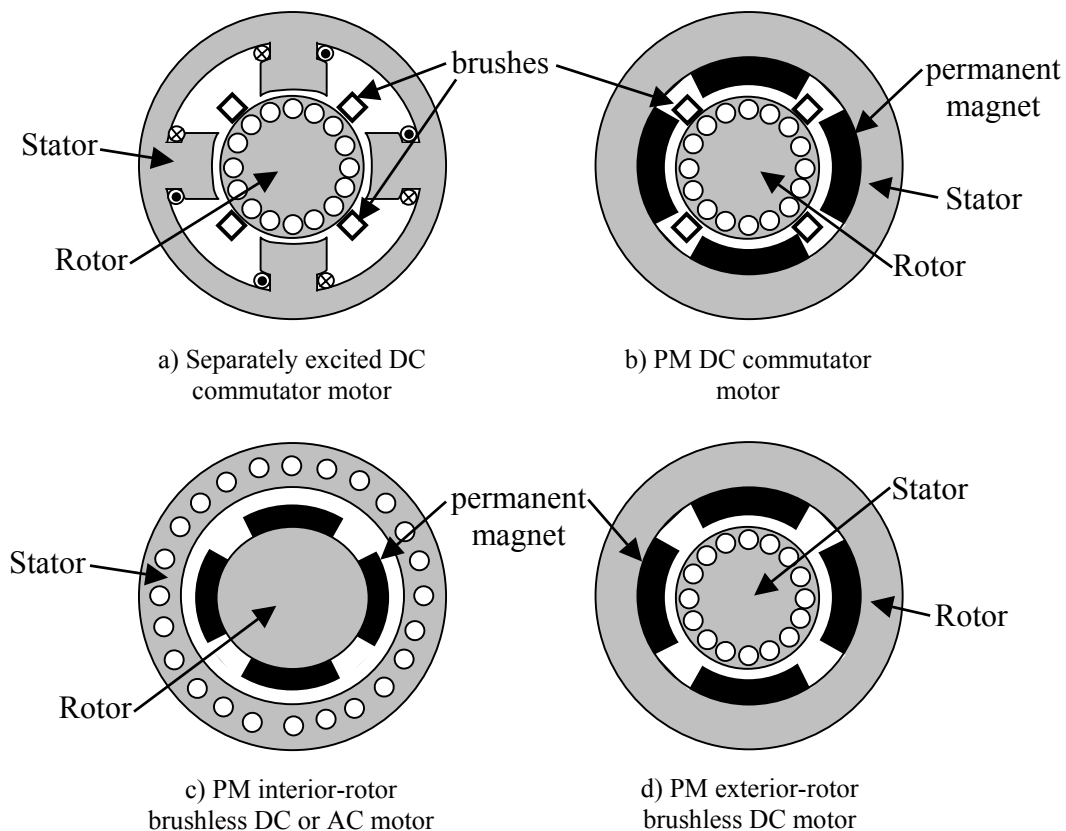


Figure 2-4 Coherence between different motors

Figure 2-4 a) shows the cross-section of a separately excited DC commutator motor (as introduced in section 2.1). The excitation flux is produced by the field windings which are wound around the main poles on the stator. The armature windings are connected to the power supply by the brushes and the commutator. The excitation field is fixed in space.

The cross-section of a permanent magnet DC commutator motor is shown in Figure 2-4 b). The magnets are fixed inside the stator frame, while the rotor carries the windings. The armature windings are connected to the power supply by the brushes and the commutator. In the DC machine, the armature field is fixed in space, even though the conductors physically rotate.

If one compares with Figure 2-4 d), the commutator and the brushes are replaced by power electronic switches and one obtains an exterior-rotor brushless DC motor. The now fixed armature windings on the stator and rotating magnets on the outside cause a rotating magnetic field.

Figure 2-4 c) shows the cross-section of a typical permanent magnet interior-rotor brushless motor (exemplified on a surface-mounted PM-motor SMPM). The magnets are on the rotating rotor and allow a small rotor diameter. This reduces the inertia compared to that of the exterior-rotor motor. Mechanical brushes and the commutator are not necessary because the windings are in the stator and do not rotate. The stator is similar to that of an AC induction motor.

According to [2], there is some confusion concerning the distinction between brushless DC and brushless AC motors. In the following paragraph, differences are pointed out and the naming is explained.

The brushless DC motor is essentially configured as a permanent magnet rotating past a set of current-carrying conductors. In order to ensure that the torque is unidirectional, the current in the conductors must reverse polarity every time a magnet pole passes by. The polarity reversal is performed by power transistors being switched corresponding to the rotor position. The phase currents are therefore square-waves and the induced voltages are trapezoidal.

In contrast, the phase currents of the brushless AC motor are sinewaves. The induced voltage should ideally be sinusoidal too. The sinewave motor operates with a rotating ampere-conductor distribution, similar to the rotating magnetic field in the induction motor or the AC synchronous machine. Therefore it is called a brushless synchronous AC motor in this thesis.

2.2.2 Main classes of synchronous AC motors

Brushless synchronous AC motors are one type of synchronous motors. Synchronous AC motors are sinusoidal current-driven machines that use a quasi-sinusoidal distributed AC stator winding and inverter. The three main types are shown in Figure 2-5.

Figure 2-5 a) shows the cross-section of a surface-mounted PM-motor (SMPM). Radial or straight-through magnetised permanent magnets are fixed to an iron rotor core. The magnets are normally glued to the rotor surface and bandaged with e.g. glass-fibre to ensure mechanical strength. Due to its isotropic¹ rotor, the d- and q-axis inductances are identical and the saliency ratio ($\xi = L_q/L_d$) is 1. Therefore no reluctance torque occurs.

¹ As the relative permeability of a permanent magnet is very nearly unity, the magnet space behaves like air. Thus the surface magnet motor exhibits negligible saliency.

In Figure 2-5 b), a possible design of an interior permanent magnet motor (IPM) is presented, in which the magnets are buried in the rotor core. Setting the magnets inside the rotor improves the mechanical strength and magnetic protection. By appropriate positioning of the permanent magnets (and additional flux barriers), the saliency ratio ξ of the IPM is varied accordingly. An IPM motor exhibits both magnetic and reluctance torque².

Figure 2-5 c) shows the cross-section of a synchronous reluctance motor. Without permanent magnets, the reluctance motor produces only reluctance torque (referring to Equation 2-6).

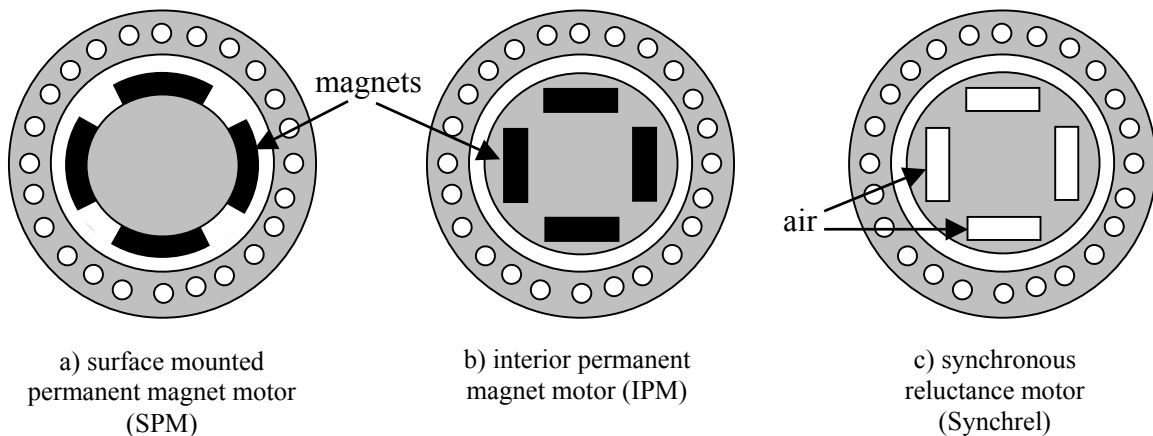


Figure 2-5 Cross-sections of the three main types of synchronous AC motors

As stated in [1], five main classes of synchronous AC motor drives can be defined, based on whether there is a theoretical finite maximum speed limit owing to voltage-limit constraints (see Figure 2-9). These are:

- (i) Finite maximum speed SMPM drive
- (ii) Infinite maximum speed SMPM drive
- (iii) Infinite maximum speed Synchrel³
- (iv) Finite maximum speed IPM drive
- (v) Infinite maximum speed IPM drive

2.2.3 IPM parameter plane

This section introduces the concept of the IPM parameter plane. This is a means for graphically visualising the effect of parameter changes on the field-weakening performance of lossless, constant parameter (interior) permanent magnet motor drives. The concept of the IPM parameter plane was first introduced by Soong and Miller [1].

² In this context, the word "hybrid" is sometimes used in literature

³ Note that all synchronous reluctance drives have infinite theoretical maximum speed and that this does not necessarily imply good field-weakening performance as the output power may be very low at high speeds.

The idea of the IPM parameter plane is to show the shape of the power against speed characteristic of an IPM in dependency of two independent parameters. The normalised magnet flux linkage Ψ_{mn} represents its SMPM nature (see chapter 3.1 for details about the normalisation). Thus the different SMPM designs are located along the x-axis of Figure 2-6, where ξ is 1 and Ψ_{mn} increases as the thickness of the magnets increases. The other parameter, the saliency factor ξ , represents the synchronous reluctance nature of the IPM. Consequently, pure synchronous reluctance designs lie on the y-axis.

Each point on the IPM parameter plane corresponds to a particular shape of normalised power against speed characteristic as shown in Figure 2-6. The ideal field-weakening performance is shown as a dashed line. On the left of the plane, the performance of synchronous reluctance motors improves with increasing saliency ratio. Designs with a high degree of permanent magnet nature lie on the right-hand side of the plane. These offer unity inverter utilisation but also have no constant-power speed range. As the reluctance nature increases and the design move to the left, the field-weakening performance improves substantially. Note that the designs on a line from the top left to bottom right of the IPM parameter plane show excellent field-weakening performance.

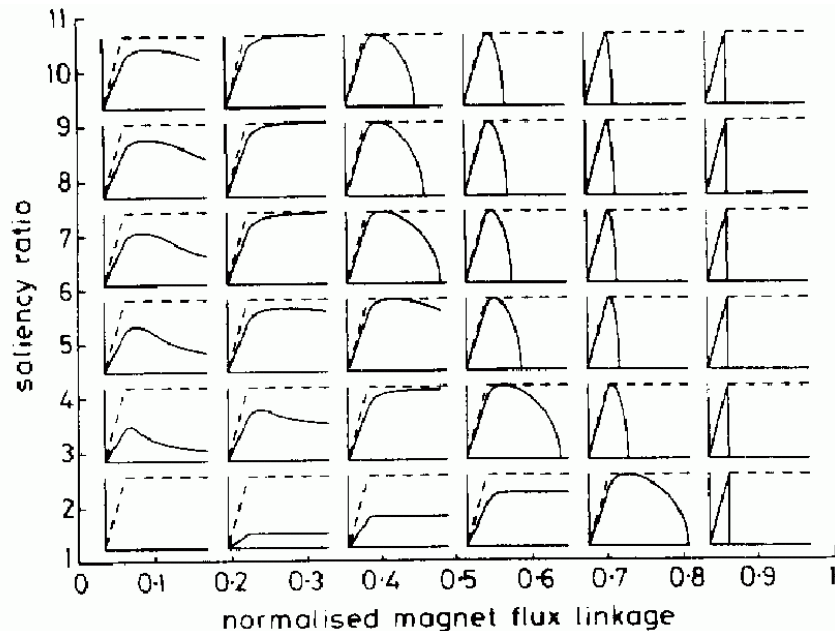


Figure 2-6 IPM parameter plane: Normalised power against speed characteristics based on Soong's study [1]

2.3 Field-weakening operation of Permanent Magnet Motors

The separately excited DC machine has separate windings for the excitation and torque-producing currents (as seen in section 2.1). Permanent magnet synchronous motors have a single stator winding which generates a current phasor I . This current phasor can be split into the two components in d- and q-axis, I_d and I_q .

$$I = \sqrt{I_d^2 + I_q^2}$$

Equation 2-4

In permanent magnet machines the flux is produced by magnets. Hence the magnetic (excitation) field or flux can not be controlled by varying the field current. The permanent magnets can be pictured as “fixed excitation flux” sources Ψ_m . However, flux control (or field-weakening) is achieved by introducing an imposing field Ψ_F against the fixed excitation from the magnets⁴. It is achieved by injecting a negative d-current I_d (or field current I_F), as shown in Figure 2-7.

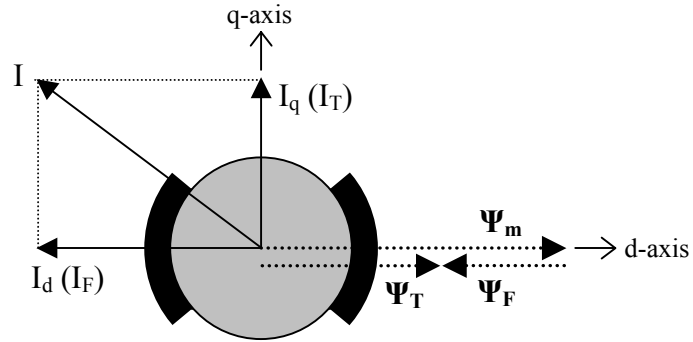


Figure 2-7 Flux-weakening of permanent magnet motors

The concept of using an imposing field can be further explained with a simple vector diagram. Figure 2-8 a) shows the voltage phasor diagram when the motor is running at a low speed well below the rated speed. When the motor is operated at rated conditions, as shown in Figure 2-8 b), it can be noted that the voltage vector is on the voltage limit contour (maximum possible voltage U_b). It is virtually impossible to increase the speed with keeping a current I in the q-axis once the induced voltage E equals the rated voltage. In order to increase the speed beyond this limit, the current phasor can be rotated towards the negative d-axis (introduction of a negative d-axis current I_d). Figure 2-8 c) shows that the voltage vector U is kept within the voltage limit.

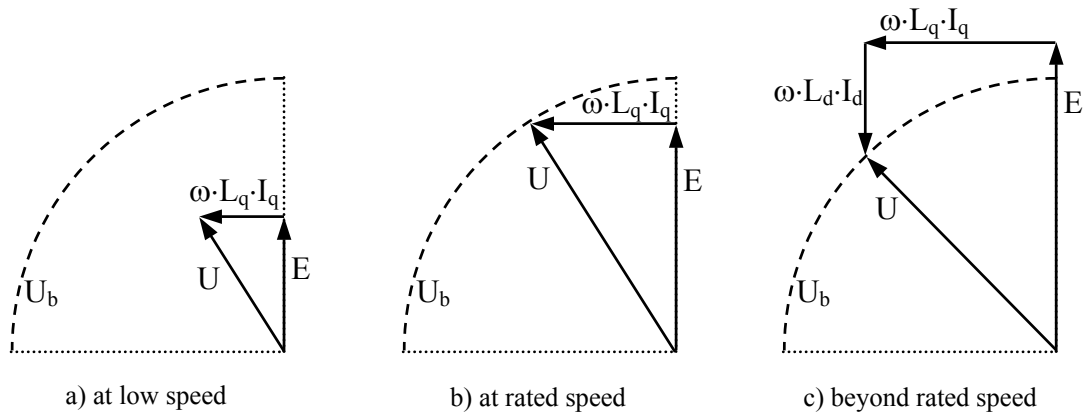


Figure 2-8 Voltage phasor diagram of the PM motor at ideal conditions

⁴ To avoid a permanent magnet irreversible demagnetisation, the decrease of the flux density must be limited. See section 4.1.4 for further information.

The voltage limit U_b of the PM motor can be expressed as

$$U_b^2 \geq \omega^2 \cdot \left[(\Psi_m + L_d \cdot I_d)^2 + (L_q \cdot I_q)^2 \right] \quad \text{Equation 2-5}$$

where ω is the electrical operating speed, Ψ_m is the magnet flux, L_d and L_q are the d-axis and q-axis synchronous inductances.

The torque equation of a PM motor can generally be expressed as

$$T = \Psi_m \cdot I_q + (L_d - L_q) \cdot I_d \cdot I_q \quad \text{Equation 2-6}$$

One can notice that the generated torque comprises two parts, the magnet torque and the reluctance torque. The total torque varies according to machine parameters as the saliency ratio ξ or the magnet thickness (defining the magnet flux Ψ_m).

The output power is from the shaft torque T and the electrical speed ω

$$P_{out} = T \cdot \omega \quad \text{Equation 2-7}$$

2.3.1 Optimal field-weakening operation

The optimal field-weakening design criterion was first introduced by Schifferl and Lipo [3]. This criterion makes the magnet flux-linkage Ψ_m equal to the maximum d-axis stator flux-linkage:

$$\Psi_m = L_d \cdot I_b \quad \text{Equation 2-8}$$

where I_b is the rated stator current. The flux in the motor gets zero when rated current is applied to the d-axis of the motor, infinite maximum speed can then be achieved.

The optimal field-weakening performance consists of an infinite constant-power speed range, an inverter utilisation of approximately 0.7 and unity normalised high-speed output power. This is achieved by designs which lie on the optimal IPM design line. The location of the optimal design line and the five drive classes (introduced in chapter 2.2.2) are shown in Figure 2-9. The optimum field-weakening performance can be obtained from any drive design lying on the optimal IPM design line. These designs fall into three categories:

- (i) Synchronous reluctance motor drives with infinite saliency.⁵
- (ii) Interior permanent magnet motor drives where $\Psi_m = L_d \cdot I_b$.
- (iii) Surface permanent magnet motor drives where $\Psi_m = 1/\sqrt{2}$.

⁵ Clearly, infinite saliency ratio synchronous reluctance motor drives are impossible. However, practical high-saliency designs may offer sufficiently good field-weakening performance. Note that the ideal constant-power speed range of a synchronous reluctance motor drive is approximately half the saliency ratio (according to [1]).

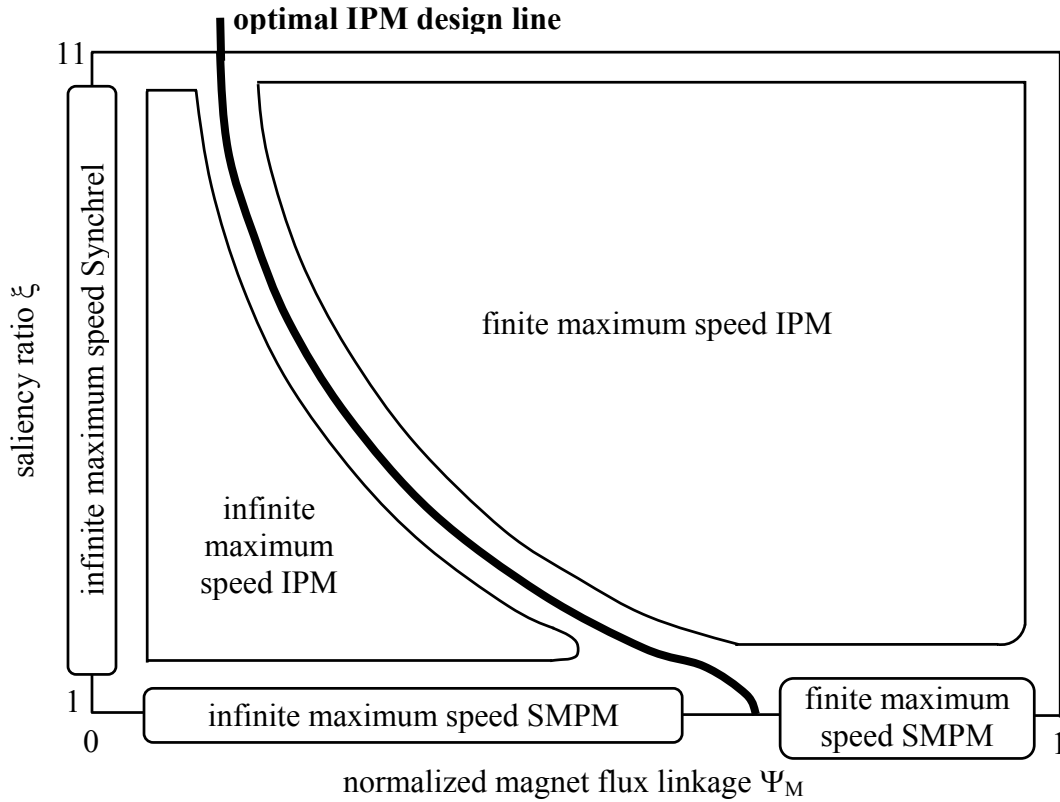


Figure 2-9 Optimal IPM design line

2.4 Practical limitations and factors

This section explores the effect of practical factors such as stator resistance, magnetic saturation or iron losses on the actual field-weakening performance. This section is based on Soong's study [1].

	2 kW SMPM		120 W Synchrel	
	T_b	CPSR	T_b	CPSR
	%	%	%	%
Copper loss	0	0	0	0
Saturation	-0.2	+8	-20	-35
Iron loss	-1.6	-3	-7	+4

Table 2-1 Effects of practical factors according to Soong [1]

The calculated effects of stator resistance, magnetic saturation and iron loss on the rated torque T_b and constant-power speed range of a 2 kW SMPM and a 120 W axially-laminated synchronous reluctance motor are shown in Table 2-1 [1]. This shows that the stator copper losses and iron losses reduce the rated torque slightly but have no first-order effect on the constant-power speed range. Especially the SMPM is relatively insensitive to practical factors, synchronous reluctance designs are sensitive to saturation.

Up to this point it has been assumed that the inductances are constant. In general, this is far from the case and the inductances are functions of the currents in both axes. Saturation describes the effect of a current in an axis on the inductance in that axis. Figure 2-10 shows a possible dependency of the q-axis induction L_q on the q-axis current I_q for unsaturated (dashed line) and saturated (solid line) conditions. Furthermore, cross-coupling is the effect of a current in an axis on the inductance in the other axis. When designing a motor it can be important to take these practical factors into account.

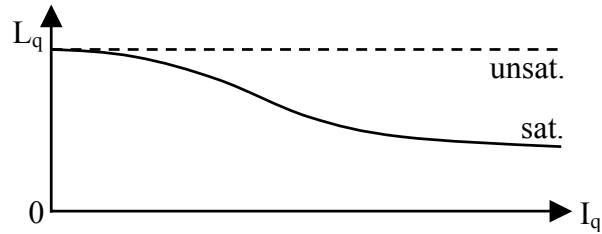


Figure 2-10 Effect of magnetic saturation on q-axis inductance

3 The SMPM drive

This chapter deals with the surface-mounted PM-motor (SMPM). At first, a common normalisation is introduced. The maximum field-weakening control for SMPM drives is then explained. Some final considerations about the SMPM characteristics conclude this chapter.

A SMPM radial flux machine with classical winding and lamination has been chosen due to the following reasons:

- The SMPM drive with a saliency ratio $\xi=1$ and thus without reluctance torque is simpler to analyse and design than an IPM drive. Within the scope of this master project it was decided that the design process of a SMPM drive would best fit the needs and the time frame given.
- As mentioned before, this master project is embedded in a project, involving several companies. The possibilities and limitations of the SMPM designs should be acquired in this master project to allow the comparison to the more promising IPM design.
- The topology of a radial flux machine with classical winding and lamination has been chosen because of the well-known and established technology and the possibility of using an existing stator lamination as potential alternative (from the induction motor which should be replaced by the PM-motor).

3.1 Normalisation

For the sake of generality, all quantities are given in normalised values referring them to base quantities. The base quantities are assumed as follows:

- The base torque T_b is the limit torque of the constant torque region, which is the rated torque.
- The base angular frequency ω_b is the maximum electrical speed of the constant torque region (base or rated speed)
- The base voltage U_b is the voltage amplitude (of the space vector) under base torque ($T=T_b$) and base angular frequency ($\omega = \omega_b$). The base voltage is also referred to as rated voltage.

The normalised quantities (subscript n indicates normalised parameters) are therefore expressed by the following equations according to Bianchi and Bolognani [6].

$$T_n = T / T_b \quad \text{Equation 3-1}$$

$$\omega_n = \omega / \omega_b \quad \text{Equation 3-2}$$

$$U_n = U / U_b \quad \text{Equation 3-3}$$

$$I_n = I / I_b, I_b = \frac{4 \cdot T_b \cdot \omega_b}{3 \cdot p \cdot U_b} \quad \text{Equation 3-4}$$

$$L_n = L / L_b, L_b = \frac{3 \cdot p \cdot U_b^2}{4 \cdot T_b \cdot \omega_b^2} \quad \text{Equation 3-5}$$

$$\Psi_{mn} = \Psi_m / \Psi_b, \Psi_b = L_b \cdot I_b = \frac{U_b}{\omega_b} \quad \text{Equation 3-6}$$

where p is the number of poles of the motor. As far as the current and the motor parameters (Equation 3-4 to Equation 3-6) are concerned, their base values are derived from the power balance (presuming ideal conditions without losses or leakage)

$$T_b \cdot \frac{2 \cdot \omega_b}{p} = \frac{3}{2} \cdot U_b \cdot I_b \quad \text{Equation 3-7}$$

With this normalisation and the choice of the magnet flux on the d-axis, the motor equations become

$$U_n^2 = \omega_n^2 \cdot \left[(\Psi_{mn} + L_n \cdot I_{dn})^2 + (L_n \cdot I_{qn})^2 \right] \quad \text{Equation 3-8}$$

$$T_n = \Psi_{mn} \cdot I_{qn} \quad \text{Equation 3-9}$$

3.1.1 Operation at rated speed

This subsection illustrates the operation at rated (or base) speed. This operation point is characterized by:

- Normalized rated torque $T_n = 1$
- Normalized electrical base speed $\omega_n = 1$
- Normalized rated voltage $U_n = 1$
- The q-axis current is set to $I_{qn} = I_n$ and the d-axis current is set to $I_{dn} = 0$ to receive the maximum torque-to-current ratio (see chapter 3.2 about the maximum field-weakening control for more details)

Solving the voltage (Equation 3-8) and torque equation (Equation 3-9) of the SMPM drive, the motor inductance and the drive current can be analytically obtained as a function of the normalised magnet flux Ψ_{mn} .

$$L_n = \Psi_{mn} \cdot \sqrt{1 - \Psi_{mn}^2} \quad (= L_{dn} = L_{qn}) \quad \text{Equation 3-10}$$

$$I_n = \frac{1}{\Psi_{mn}} \quad \text{Equation 3-11}$$

3.2 Maximum torque field-weakening control

In this section, the particular field-weakening control strategy to obtain maximum torque (and hence power) at any speed within the inverter volt-ampere rating of the SMPM drive is presented. This section is based on the studies of Soong [1] and Morimoto [13].

The circle diagram is a well known graphical technique for determining the maximum torque field-weakening control strategy for synchronous motor drives. These drives are usually current controlled and so it is convenient to define an operating point in terms of its location in the (I_d , I_q)-plane. The current limit constraint $I_{qn}^2 + I_{dn}^2 \leq I_n^2$ forms a circle in this plane. From Equation 3-8 it can be shown that the voltage limit constraint $V_n \leq 1$ defines a circle whose centre is offset from the origin (see Figure 3-1). The size of this circle is inversely proportional to speed. Its centre is termed the infinite-speed operation point as the operating point must converge towards it at high speed. A given operating point will not exceed the voltage- or current-limit constraint if it lies within the intersection of the voltage- and the current-limit circle. From Equation 3-9 it can be shown that lines of constant torque form straight lines parallel to the d-axis (see Figure 3-1).

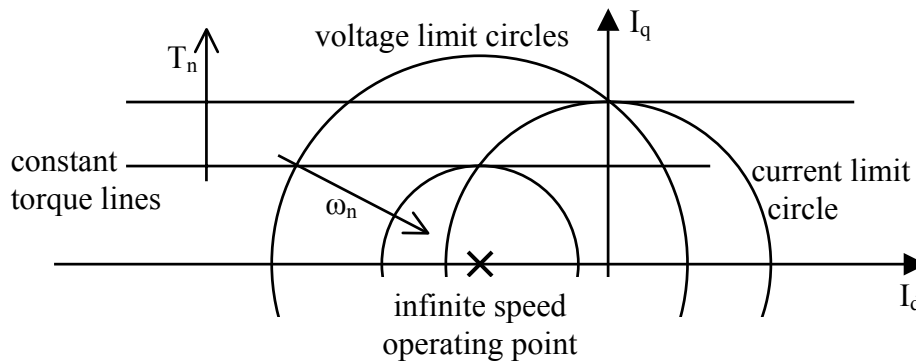


Figure 3-1 Circle diagram for SMPM

A simpler circle diagram for a finite and infinite maximum speed SMPM drive showing the maximum torque field-weakening control strategy is given in Figure 3-2. The three operation modes (corresponding to the numbers in Figure 3-2) are:

(i) Mode 1: *current limited region*. This is the region from zero to rated speed where maximum torque is obtained by operating with normalised rated current I_n in the q-axis. The dots in Figure 3-2 show the mode 1 maximum-torque-per-ampere operating points.

(ii) Mode 2: *current-and-voltage-limited region*. Above rated speed, the drive is operated with rated current at the minimum current angle⁶ required to give rated terminal voltage. The optimised current angle can be determined from Equation 3-8:

⁶ The current angle γ is defined as the angle by which the stator current leads the q-axis. Thus $I_{qn} = I_n \cdot \cos \gamma$ and $I_{dn} = -I_n \cdot \sin \gamma$.

$$\gamma_{opt2} = \sin^{-1} \left(\frac{\omega_n^2 \cdot \Psi_{mn}^2 + \omega_n^2 \cdot \left(\frac{L_n}{\Psi_{mn}} \right)^2 - 1}{2 \cdot \omega_n^2 \cdot L_n} \right) \quad \text{Equation 3-12}$$

(iii) Mode 3: *voltage limited region*. Here the drive operates to give maximum torque with a limited voltage. The optimised current angle for mode 3 can be determined as:

$$\gamma_{opt3} = \tan^{-1}(-\omega_n \cdot \Psi_{mn}) \quad \text{Equation 3-13}$$

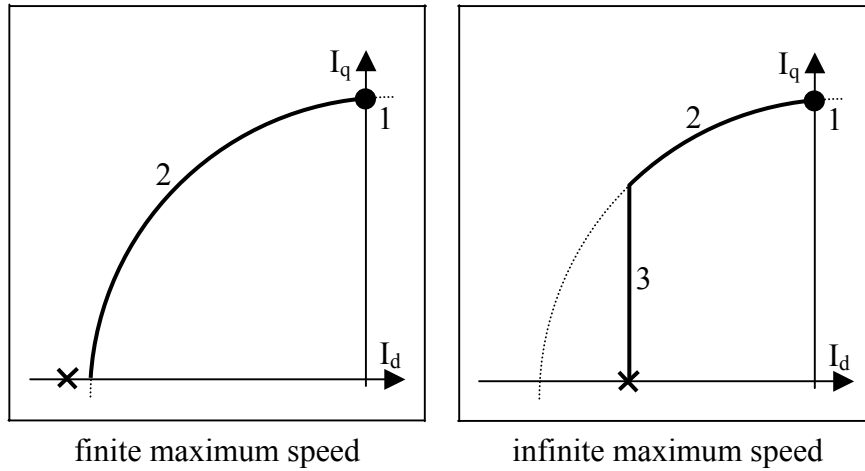


Figure 3-2 Maximum torque field-weakening control strategies for SPM

For finite maximum speed drives (see left side of Figure 3-2) the infinite speed operating point (marked 'x') lies outside the current-limited circle. This is the case if the normalised magnet flux is bigger than 0.71 ($\Psi_{mn} > 1/\sqrt{2}$). If so, mode 3 does not appear and the maximum speed is limited to:

$$\omega_{max} = \frac{1}{\Psi_{mn} - \sqrt{1 - \Psi_{mn}^2}} \quad \text{Equation 3-14}$$

The maximum field-weakening speed ω_{max} is not limited if the infinite speed operating point (characterised by $I_{dn} = -\Psi_{mn}/L_n$) lies inside the current limit circle. In this case the normalised magnet flux is smaller than 0.71 ($\Psi_{mn} \leq 1/\sqrt{2}$).

3.3 SMPM characteristics

The shape of the normalised torque against speed characteristic of the SMPM can be characterised by one parameter. The choice of the parameter is arbitrary, but a useful selection is the normalised magnet flux linkage Ψ_{mn} for the SMPM. The normalised power against speed characteristic for the lossless, constant parameter SMPM drive is shown in Figure 3-3.

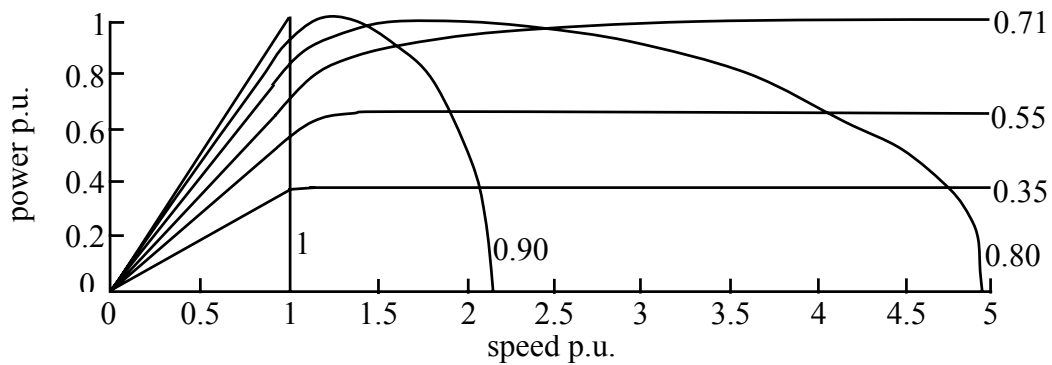


Figure 3-3 Normalised power against speed characteristic as function of normalized magnet-flux linkage

A SMPM with Ψ_{mn} equal to unity has unity inverter utilisation (normalised output power at rated speed) but has no field-weakening capability. As the inductance increases and Ψ_{mn} decreases, the inverter utilisation decreases slightly but the field-weakening performance improves considerably. Optimum field-weakening performance is obtained with $\Psi_{mn} = 1/\sqrt{2}$, in which case the normalised output power approaches unity at high speed. Decreasing Ψ_{mn} further ($\Psi_{mn} < 1/\sqrt{2}$) decreases the achievable output power level.

Commercial surface mounted permanent magnet designs generally have values of Ψ_{mn} between 0.83 and 0.96. The constant-power speed range is usually lower than 2:1. A wider constant-power speed range can be achieved by adding series inductors but at the cost of extra weight, volume and losses [4].

4 Analytical Design

This chapter concentrates on the analytical design of a SMPM. Specific parameter coherences are shown and general design reflections are outlined. An adequate analytical loss model is derived and used in the design process. Additional considerations on the armature reaction and the magnet protection are also discussed. In section 4.2, different designs are investigated.

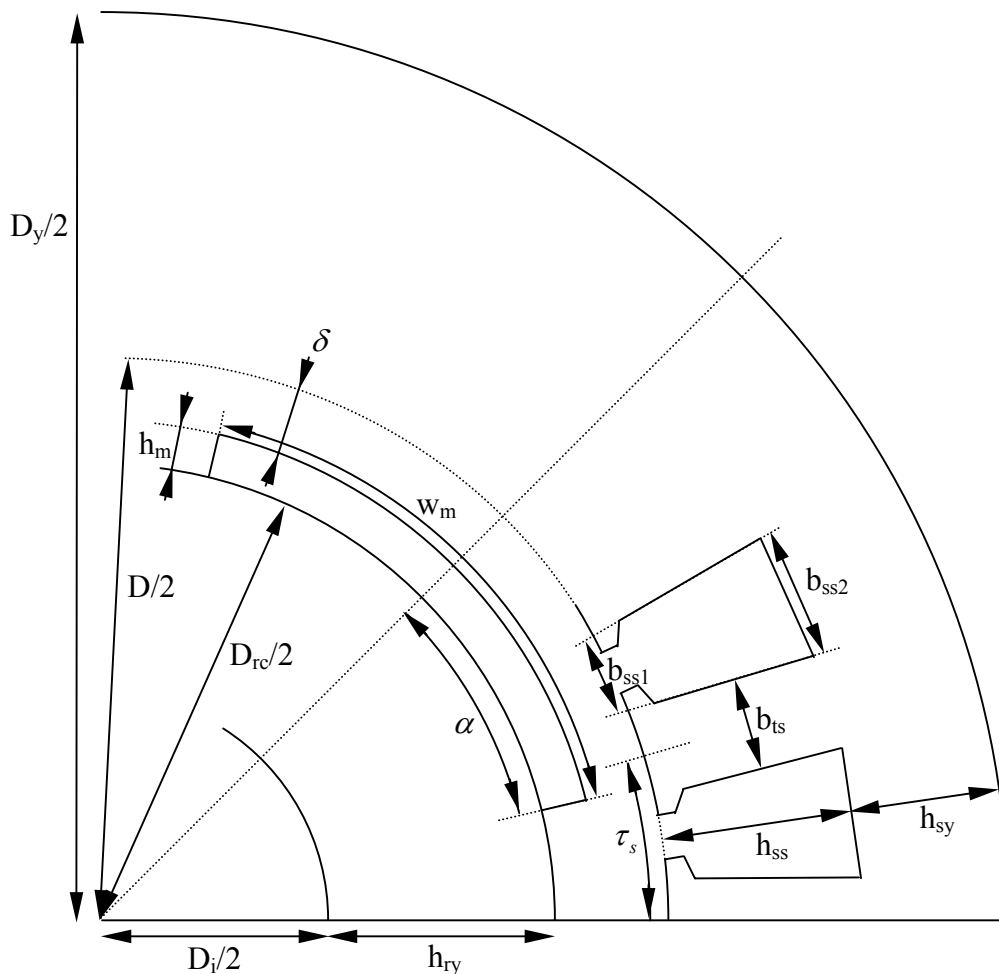


Figure 4-1 Cross section of a 4-pole SMPM with dimensions

Figure 4-1 shows a cross-section of one pole of a four pole SMPM. Relevant geometrical parameters are also shown in the scheme.

The following section focuses on the design of the surface-mounted PM-motor. It is the simplest type of the PM machine design. There are several aspects that must be taken into considerations when designing a PM-machine. Essential criterions such as the choice of magnets, their arrangement (salient/non-salient rotor) and the protection against demagnetisation (regarding overload and thermal capability) are discussed.

The design process starts with the definition of the constraints and the requirements of operation. In this study, the design specifications are:

- A rated torque of 60 Nm at a rated speed of 1500 rpm is required.
- The field-weakening range should be up to 3, corresponding to a maximum speed of 4500 rpm.

Some constraints and target values are listed below:

- The inverter output line-to-line voltage is roughly limited to a rms-value of $U_{L-L}=35$ V. That corresponds to a peak value of the phase voltage \hat{U} of about 28.6 V ($\hat{U} = U_{L-L} \cdot \sqrt{2} / \sqrt{3}$).
- The outer dimensions of the SMPM drive are restricted to the dimension of the induction motor that shall be replaced.
 - the total length is restricted to $l = 0.34$ m
 - the outer stator diameter is restricted to $D_y = 0.24$ m
 The frame and the bearings are included in the outer dimension and reduce the effective motor dimension to $l = 0.165$ m.
- The magnet characteristics are assumed as follows:
 - remanence flux density $B_r = 1.1$ T
 - demagnetisation flux density $B_D = -0.2$ T
 - relative magnet permeability $\mu_r = 1.05$
- A reasonable design has the following flux densities:
 - fundamental airgap flux density $\hat{B}_\delta \approx 0.85 - 0.95$ T
 - maximum flux density in the rotor yoke $B_{ry} \approx 1.4$ T
 - maximum flux density in the stator yoke $B_{sy} \approx 1.4$ T
 - maximum flux density in the stator teeth $B_{st} \approx 1.8$ T (near to saturation)
- To prevent high temperatures and insulation problems, the maximum current density J should be lower than 7 A/mm^2 . This value is relevant for a motor without forced cooling. Depending on the way the motor is cooled, higher current densities can be possible.

4.1 Design process

The maximum value of the flux density in the airgap above the magnets (B_m) is given by the following equation. It is assumed that the magnets are radially magnetised (see App. D).

$$B_m = \frac{B_r \cdot k_{leak}}{1 + \frac{\mu_r \cdot \delta_e}{h_m}} \quad \text{Equation 4-1}$$

where δ_e is the equivalent airgap length (see Equation 4-3) and h_m is the magnet thickness. The factor k_{leak} is the ratio of the flux coupled with the stator windings to the total magnet flux. Consequently, k_{leak} is an empirical constant for taking the rotor flux

leakage into account. The temperature dependency and the curvature of the airgap are not considered in Equation 4-1. A more accurate equation considering that the airgap is curved is presented in [7]. The following equation is given

$$B_m(r) = \frac{h_m \cdot B_r}{r \cdot \left[\ln\left(\frac{D_{rc} + 2 \cdot h_m}{D_{rc}}\right) + \mu_r \cdot \ln\left(\frac{D_{rc} + 2 \cdot h_m + 2 \cdot \delta_e}{D_{rc} + 2 \cdot h_m}\right) \right]} \quad \text{Equation 4-2}$$

where D_{rc} is the rotor core diameter. The parameter r stands for the radius at which the flux density is calculated. The equivalent airgap length is given by

$$\delta_e = k_{carter} \cdot \delta \quad \text{Equation 4-3}$$

which takes into account the effect of a slotted stator using the Carter factor k_{carter} [8]

$$k_{carter} = \frac{\tau_s}{\tau_s - \kappa \cdot \delta}, \text{ where}$$

$$\kappa = \frac{4}{\pi} \cdot \left[\frac{b_{ss1} \cdot k_{open}}{2 \cdot \delta} \cdot \arctan\left(\frac{b_{ss1} \cdot k_{open}}{2 \cdot \delta}\right) - \ln \sqrt{1 + \left(\frac{b_{ss1} \cdot k_{open}}{2 \cdot \delta}\right)^2} \right]. \quad \text{Equation 4-4}$$

The definitions of the stator slot pitch τ_s , the inner stator slot width b_{ss1} and the stator opening factor k_{open} are shown in Figure 4-2. The stator slot pitch is calculated from the inner stator diameter (D) and the number of stator slots (Q_s) as follows

$$\tau_s = \pi \cdot \frac{D - \delta}{Q_s} \quad \text{Equation 4-5}$$

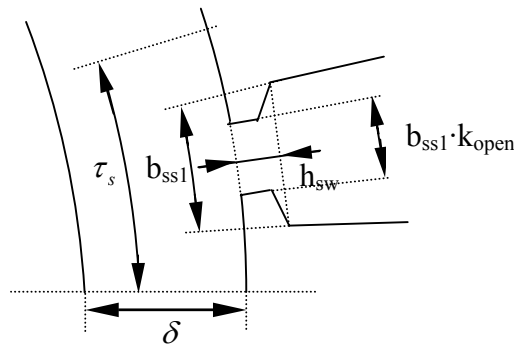


Figure 4-2 Illustration of the dimensions in the area of the stator slot opening

The airgap length δ can be chosen more freely in a PM-machine compared to an induction machine⁷. The physical airgap length in PM-machines is in the range of 1-3 mm, including a layer of bandage that is used to fix and protect the magnets.

⁷ In an induction machine the airgap is kept small to limit the magnetising current and to improve the power factor $\cos\phi$.

The larger the airgap, the more magnet material is needed to produce the required airgap flux density. More magnet material implies not only a higher cost, but also a larger effective airgap⁸. Consequently, an increase in the airgap results in a decrease of the magnetising inductance of the machine. As mentioned in chapter 3, the field-weakening range depends primarily on the inductance; a decrease of the inductance is the same as a decrease of the field-weakening range.

The positive effect of having a large airgap is that it gives a more sinusoidal flux distribution in the airgap, which results in a very small variation of flux density in the magnets and on the rotor surface. Thus, the eddy current losses (which are a function of the time rate of change of the vector flux density) can be significantly reduced. More details on the loss calculation can be found later in section 4.1.3.

The airgap for field-weakening applications should be designed as small as possible. Going to the mechanical limits of feasibility, the required magnet material can be minimized and the inductance of the machine can be maximized to allow widest possible field-weakening range.

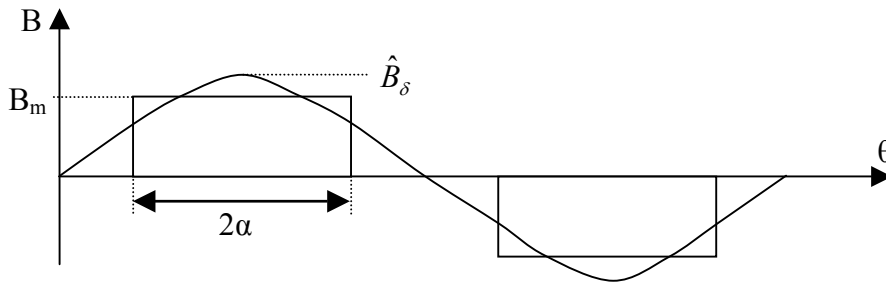


Figure 4-3 Actual and fundamental airgap flux density

Let us assume the airgap flux density has a rectangular shape as shown in Figure 4-3. The fundamental airgap flux density (B_{δ}) is then calculated to

$$\hat{B}_{\delta} = \frac{4}{\pi} \cdot B_m \cdot \sin \alpha \quad \text{Equation 4-6}$$

where α is the half pole angle defined in electrical degrees:

$$\alpha = \frac{w_m \cdot p}{2 \cdot (D - 2 \cdot \delta)} \quad \text{Equation 4-7}$$

The pole angle (2α) is two times the half pole angle and is normally chosen close to $2\pi/3$ electrical degrees (120°). This can be explained by studying the fundamental component of the airgap flux density and its contribution to the torque of the motor. An increase of the pole angle to 180° creates a 14 % higher airgap flux density as can be derived from Equation 4-6, while the magnet volume increases by 50 %, which will approximately increase the cost of the magnets by the same percentage [8].

⁸ The effective airgap includes the equivalent airgap and the magnet height ($\delta_c + h_m / \mu_r$)

The magnet coverage cov (in percentage of the rotor core circumference) can then be expressed as follows⁹

$$\text{cov} = \frac{2 \cdot \alpha}{\pi} = \frac{w_m \cdot p}{\pi \cdot (D - 2 \cdot \delta)} \quad \text{Equation 4-8}$$

4.1.1 Magnetic design

This section describes the guidance of the magnetic flux in the motor. The iron cross-sections are calculated to keep the flux density in the constraints given at the beginning of chapter 4.

Ignoring the leakage, the total magnetic flux per pole Φ_{mp} produced by the magnets is given by

$$\Phi_{mp} = B_m \cdot w_m \cdot l = B_m \cdot \frac{2 \cdot \alpha}{p} \cdot (D - 2 \cdot \delta) \cdot l \quad \text{Equation 4-9}$$

The maximum flux in the stator yoke (Φ_{sy}) is one half of the flux produced by the magnets and can be expressed as follows

$$\Phi_{sy} = \frac{\Phi_{mp}}{2} = B_{sy} \cdot h_{sy} \cdot k_j \cdot l \quad \text{Equation 4-10}$$

where B_{sy} is the maximum flux density in the stator yoke, h_{sy} is the height of the stator yoke and k_j is the stacking factor of the stator iron laminations. Combining Equation 4-9 and Equation 4-10, the height of the stator yoke h_{sy} can be calculated for a fixed stator yoke flux density B_{sy} as

$$h_{sy} = \frac{\alpha \cdot B_m \cdot (D - 2 \cdot \delta)}{p \cdot k_j \cdot B_{sy}} \quad \text{Equation 4-11}$$

Similarly, for a fixed maximum rotor yoke flux density B_{ry} , the height of the rotor yoke h_{ry} can be calculated as

$$h_{ry} = \frac{\alpha \cdot B_m \cdot (D - 2 \cdot \delta)}{p \cdot k_j \cdot B_{ry}} \quad \text{Equation 4-12}$$

For the calculation of the stator tooth width, it is assumed that all the magnet flux passes through the stator teeth. After several conversions, the stator tooth width b_{ts} can be expressed for a fixed maximum stator teeth flux density B_{st} as in Equation 4-13.

⁹ Please notice that the minimum arc length of the magnet (inside arc) must be used to calculate the magnet pole area from the magnet coverage cov .

$$b_{ts} = \frac{B_m \cdot \pi \cdot (D - 2 \cdot \delta)}{Q_s \cdot k_j \cdot B_{st}} \quad \text{Equation 4-13}$$

If the iron cross-sections that guide the magnetic flux are calculated, the additional dimensions of the motor design (e.g. stator slot height h_{ss} , shaft diameter D_i or outer stator diameter D_y) can be derived or fixed. The design then must be controlled and the outer dimensions must be compared to the constraints.

Finally, the stator slot area A_{sl} can be calculated as (see Figure 4-1 and Figure 4-2 for details about the parameters)

$$A_{sl} = \frac{b_{ss1} + b_{ss2}}{2} \cdot (h_{ss} - h_{sw}) \quad \text{Equation 4-14}$$

The copper area per slot A_{cu} can be calculated as

$$A_{cu} = f_s \cdot A_{sl} \quad \text{Equation 4-15}$$

where f_s is the fill factor of the stator winding. The fill factor takes both slot and conductor insulations as well as gaps into account. A realistic value for the fill factor f_s is in the range of 0.4 to 0.5, depending on the conductor arrangement and the insulation used. The conductor area A_{cond} is then given by the following equation (the choice of the number of conductors per stator slot n_s is derived in section 4.1.2.)

$$A_{cond} = \frac{A_{cu}}{n_s} \quad \text{Equation 4-16}$$

4.1.2 Operation performance

This section deals with the fulfillment of the operation constraints (a rated torque of 60 Nm at a rated speed of 1500 rpm is required). The torque can be expressed by the following formula

$$T = \pi \cdot \frac{(D - \delta)^2}{4} \cdot l \cdot \hat{S}_1 \cdot \hat{B}_\delta \cdot k_{w1} \cdot \sin(\beta) \quad \text{Equation 4-17}$$

where \hat{S}_1 is the peak current loading, k_{w1} is the winding factor for the first harmonic and β is the angle between the current vector and the magnet flux vector. The maximum torque is achieved for a SPM when $\beta = \pi/2$ (90°) as in Figure 4-4. This is the case for operation up to the rated speed according to the maximum torque field-weakening control introduced in section 3.2.

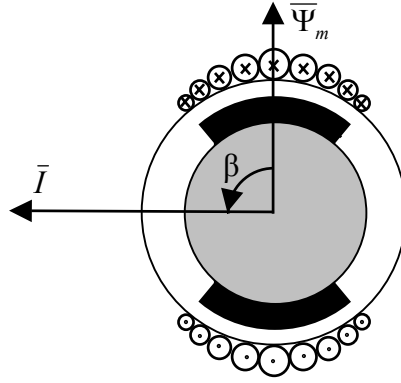


Figure 4-4 Schematic with current and airgap flux vector

The winding factor for the first harmonic k_{w1} can be calculated as

$$k_{w1} = \frac{1}{q} \cdot \frac{\sin(\pi/6)}{\sin\left(\frac{\pi}{6 \cdot q}\right)} \quad \text{Equation 4-18}$$

where q is the number of stator slots per pole per phase

$$q = \frac{Q_s}{p \cdot m} \quad \text{Equation 4-19}$$

Equation 4-17 can be used to calculate the current loading S_1 required to achieve the rated torque. The peak-value of the total stator current per slot can be derived as follows:

$$n_s \cdot \hat{I} = \hat{S}_1 \cdot \tau_s \quad \text{Equation 4-20}$$

The current density J can then be calculated from the total stator current per slot given in Equation 4-20 and the copper area per slot given in Equation 4-15. The current density should be controlled according to the constraints settled at the beginning of this chapter. If the current density is too high, adaptations in the design or forced cooling should be considered.

$$J = \frac{n_s \cdot I}{A_{cu}} \quad \text{Equation 4-21}$$

The peak value of the fundamental induced voltage E (back EMF) is given by the maximum value of the derivation of the magnet flux linkage

$$\hat{E} = \max\left[\frac{d\Psi_m}{dt}\right] = N \cdot \max\left[\frac{d\Phi_m}{dt}\right] \quad \text{Equation 4-22}$$

where N is the number of turns per phase (Equation 4-23) and Φ_m is the fundamental magnetic flux (Equation 4-24).

$$N = \frac{p}{2} \cdot q \cdot n_s \cdot k_{wl} \quad \text{Equation 4-23}$$

$$\Phi_m = \hat{\Phi}_m \cdot \sin(\omega_{el} \cdot t) = \hat{B}_\delta \cdot l \cdot \frac{(D - \delta) \cdot \pi}{p} \cdot \frac{2}{\pi} \cdot \sin(\omega_{el} \cdot t) \quad \text{Equation 4-24}$$

The electrical angular velocity ω_{el} is coupled to the electrical frequency and the mechanical angular velocity in the following relation:

$$\omega_{el} = 2 \cdot \pi \cdot f = \omega_{mech} \cdot \frac{p}{2} \quad \text{Equation 4-25}$$

Finally, the induced voltage E can be calculated as

$$\hat{E} = q \cdot n_s \cdot k_{wl} \cdot \omega_{el} \cdot \hat{B}_\delta \cdot l \cdot (D - \delta) \quad \text{Equation 4-26}$$

The power balance of the output power P_{out} is given as ($\cos(\gamma)=1$ as $I = I_q$)

$$P_{out} = \frac{3}{2} \cdot \hat{E} \cdot \hat{I} \cdot \cos(\gamma) = \frac{3}{2} \cdot \hat{E} \cdot \hat{I} = T \cdot \omega_{mech} \quad \text{Equation 4-27}$$

The magnetising inductance L_m of the motor is calculated as (refer to App. B1 for details about the calculation of the motor inductance)

$$L_m = \frac{3}{\pi} \cdot (q \cdot n_s \cdot k_{wl})^2 \cdot \frac{\mu_0}{\delta_e + \frac{l_m}{\mu_r}} \cdot (D - \delta) \cdot l \quad \text{Equation 4-28}$$

The stator leakage inductance L_{leak} can be calculated as (a detailed derivation can be found in App. B2)

$$L_{leak} = p \cdot q \cdot n_s^2 \cdot l \cdot \mu_0 \cdot \lambda_1 \quad \text{Equation 4-29}$$

where the ratio λ_1 is called the specific permeance coefficient of the slot opening. The end winding leakage reactance is neglected for simplicity.

The external voltage U (that is the inverter output voltage phasor) is calculated based on the dq-equivalent circuit from Figure 4-5. It includes the copper losses (see chapter 4.1.3 for details about the calculation) in the form of a serial resistor R_{cu} . The iron losses are not included in the equivalent circuit. The transformation of the three-phase quantities for use in the dq-equivalent circuit is done with the Park transformation (refer to App. C for details).

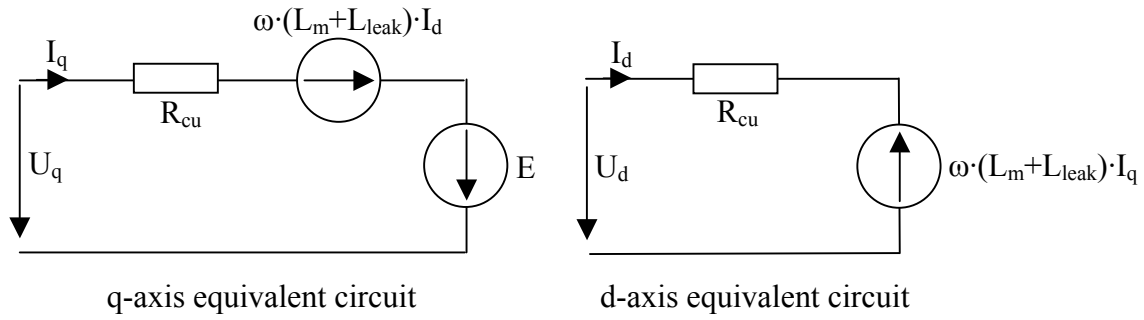


Figure 4-5 Equivalent dq-diagram

The terminal voltage at base speed U_b can be calculated as¹⁰

$$U_q = E + I \cdot R_{cu}, \quad U_d = -\omega \cdot (L_m + L_{leak}) \cdot I \tag{Equation 4-30}$$

$$U_b = \sqrt{(E + I \cdot R_{cu})^2 + \omega^2 \cdot (L_m + L_{leak})^2 \cdot I^2} \tag{Equation 4-31}$$

Figure 4-6 a) shows the vector diagram at base speed. Knowing the terminal current I and voltage U (with the phase angle), the power factor $\cos(\varphi)$ can be found as

$$\cos(\varphi) = \frac{E + I \cdot R_{cu}}{U_b} \tag{Equation 4-32}$$

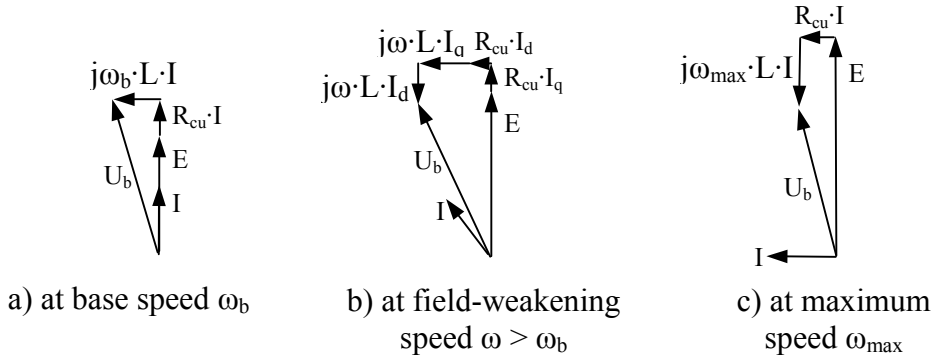


Figure 4-6 Vector diagrams at different operation points

The terminal current and voltage for every operation point can be found analytically from the dq-equivalent circuits in Figure 4-5. Figure 4-6 b) shows the vector diagram at a field-weakening speed above base speed. To determine the maximum field-weakening range, the voltage at maximum speed ω_{max} ¹¹ is calculated to

$$U_q(\omega_{max}) = E_{max} - \omega_{max} \cdot (L_m + L_{leak}) \cdot I \tag{Equation 4-33}$$

$$U_d(\omega_{max}) = -I \cdot R_{cu} \tag{Equation 4-34}$$

¹⁰ At base speed, the current lies on the q-axis ($I_q=I, I_d=0$).

¹¹ At maximum speed, the current lies on the negative d-axis ($I_q=0, I_d=-I$).

Figure 4-6 c) shows the vector diagram at maximum speed. The induced voltage E is proportional to the electrical frequency f . At maximum speed, the induced voltage is maximal as well ($E_{\max} = E \cdot f_{\max}/f_b$). The maximum field-weakening range can be determined by the constraint, that the voltage at maximum speed $U(\omega_{\max})$ is restricted to the base voltage U_b (Equation 4-31). The maximum field-weakening range can then be concluded as in Equation 4-36.

$$U_b^2 = (I \cdot R_{cu})^2 + \left(E \cdot \frac{f_{\max}}{f_b} - I \cdot 2\pi \cdot f_{\max} \cdot (L_m + L_{leak}) \right)^2 \quad \text{Equation 4-35}$$

$$\frac{f_{\max}}{f_b} = \frac{\sqrt{U_b^2 - (I \cdot R_{cu})^2}}{E - 2\pi \cdot f_b \cdot (L_m + L_{leak}) \cdot I} \quad \text{Equation 4-36}$$

In a final step, the number of conductors per stator slot n_s can be calculated to fit the voltage U to the constraints given of the inverter. This equation is not derived in this thesis because it would not be accurate enough (due to the fact that the iron losses are not taken into account). For the analytical design, a reasonable number of conductors per stator slot is chosen so that the voltage stays within the constraints.

All the equations in this chapter are derived for serial Y-connection of the winding. Another solution would be the parallel Y-connection. Changing the winding arrangement from serial to parallel windings (Y connected) has the following effects if n_s is kept constant:

- The induced voltage E is divided by c .
- The conductor current stays the same but the terminal current I is multiplied by c .
- The winding resistance R_{cu} is divided by c^2 .
- The magnetising inductance L_m and the base inductance L_b are divided by c^2 , the p.u. inductance stays the same.
- Operation performance, field-weakening range and power factor are not affected!

where c is the parallel coupling factor. Taking the example of a 4-pole machine, the number of conductors per slot n_s can be doubled for a constant induced voltage E when the winding arrangement is changed from serial to parallel Y-connection. The conductor current is divided by 2, but the terminal current as well as the current density stays constant. The only advantage of parallel Y-connection windings is the reduced diameter of the stator conductors allowing a higher fill factor f_s and therefore a reduced current density J (and reduced copper losses, see section 4.1.3). As a conclusion, the winding arrangement should be chosen as parallel Y-connected if the available voltage is low.

4.1.3 Loss models

In PM motors, stator iron losses can form a large proportion of the total losses. This is partly due to the really low rotor loss and the non-sinusoidal flux density distribution. In this section, copper and stator iron losses are calculated and a dq-equivalent circuit with the iron losses is presented. Additional losses as friction or stray losses are neglected.

The copper resistance R_{cu} of one phase of the stator winding can be calculated as¹²

$$R_{cu} = \rho_{cu} \cdot \frac{(p \cdot l + D \cdot \pi \cdot k_{coil}) \cdot n_s \cdot q}{A_{cond}} \quad \text{Equation 4-37}$$

where ρ_{cu} is the copper resistivity and k_{coil} is an empirical constant depending on the end windings arrangement. The term $(D \cdot \pi \cdot k_{coil})$ in Equation 4-37 is a factor that takes into account the length of the end windings on each side of the machine. The total copper losses P_{cu} are calculated according to Equation 4-38.

$$P_{cu} = 3 \cdot R_{cu} \cdot I^2 \quad \text{Equation 4-38}$$

Copper losses are the predominant losses at low speed. Since the current I is limited to the base current I_b , copper losses are not much influenced by increasing speed.

A possibility to minimize the copper losses is to fill the stator slots with as much copper as possible (using the maximum possible conductor diameter). Cramming copper into the slots not only reduces the current density, it also improves the thermal conduction of heat from the conductors to the lamination stack, especially when the coils are varnished or encapsulated.

An optimal analytical design tool requires good means for predicting the iron losses. Finite element analysis can produce an estimate of iron losses but it is time consuming.

In the dq-equivalent circuit, the iron loss component can be represented by a resistor in parallel to the induced voltage E and the armature reaction [11]. The copper losses P_{cu} in the stator winding are represented by a series resistor R_{cu} . The stator leakage reactance L_{leak} is integrated in the equivalent circuit in series to the copper resistance. The end winding leakage reactance is neglected. Figure 4-7 shows the equivalent dq-diagrams including the iron losses.

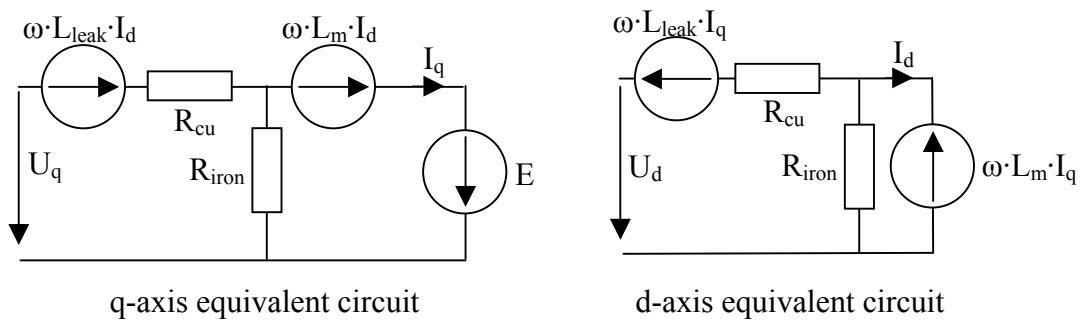


Figure 4-7 Equivalent dq-diagram with iron loss resistor R_{iron}

The iron loss resistance R_{iron} can be modelled as two parallel resistances for the eddy current and hysteresis losses (R_{eddy} and R_{hyst} respectively) as shown in Figure 4-8. The

¹² Using the formula $R = \rho \cdot L / A$, where R is the resistance, ρ is the resistivity, L is the length and A is the cross-section of the conductor.

eddy current and hysteresis resistance are calculated at no-load conditions (no current) as:

$$R_{eddy}(\omega_b) = \frac{3 \cdot E^2}{p_{eddy}(teeth) \cdot V_t + p_{eddy}(yoke) \cdot V_y} \quad \text{Equation 4-39}$$

$$R_{hyst}(\omega_b) = \frac{3 \cdot E^2}{p_{hyst}(teeth) \cdot V_t + p_{hyst}(yoke) \cdot V_y} \quad \text{Equation 4-40}$$

As the induced voltage E is proportional to the electrical frequency f and the eddy current losses are proportional to the square of the electrical frequency ($P_{eddy} \sim f^2$), the eddy current resistance R_{eddy} doesn't depend on the frequency (Equation 4-41). In contrast, the hysteresis losses are only proportional to the electrical frequency ($P_{hyst} \sim f$). The hysteresis resistance R_{hyst} therefore depends on the frequency and must be calculated for field-weakening applications according to Equation 4-42.

$$R_{eddy} = const. \quad \text{Equation 4-41}$$

$$R_{hyst} = R_{hyst}(\omega_b) \cdot \frac{f}{f_b} \quad \text{Equation 4-42}$$

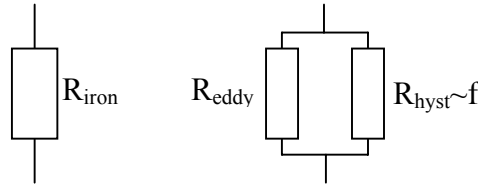


Figure 4-8 Iron loss resistance R_{iron}

To obtain the no-load iron losses, a set of improved approximate models for the prediction of iron losses based on general FEM-calculations were derived in a paper from Mi, Slemon and Bonert [9].

Core losses (or iron losses) are due to eddy currents and magnetic hysteresis in the iron laminations. The rotor core losses are usually considered to be small and negligible¹³, whereas the stator core losses in the stator teeth and stator yoke generate the main portion of the total iron losses. Measurements of iron losses in magnetic material are traditionally made with sinusoidal flux density. The total iron loss density p_{iron} is commonly expressed in the following form for sinusoidal magnetic flux density B with an angular frequency ω_{el} :

$$p_{iron} = p_{hyst} + p_{eddy} = k_{hyst} \cdot B^{\beta_{St}} \cdot \omega_{el} + k_{eddy} \cdot B^2 \cdot \omega_{el}^2 \quad \text{Equation 4-43}$$

where p_{hyst} and p_{eddy} are the hysteresis and the eddy current loss-density respectively. k_{hyst} and k_{eddy} are hysteresis and eddy current constants and β_{St} is the Steinmetz constant. All

¹³ Due to the fact that the main flux in the rotor is a DC-flux. However, potential harmonics may cause rotor eddy currents.

these constants depend on the lamination material. Typical values for grades of silicon iron laminations are in the ranges of $k_{hyst}=40-55$, $\beta_{St}=1.8-2.0$ and $k_{eddy}=0.04-0.07$.

The iron loss expression in Equation 4-43 is valid only for sinusoidal flux density. In SMPM motors, the variation in flux density in the stator core is far from sinusoidal. In this situation, the hysteresis loss is still easy to evaluate as it depends only on the peak value of the flux density assuming that there are no minor hysteresis loops. Tooth hysteresis loss and yoke hysteresis loss can be expressed simply as a function of the maximum flux density in each area. In the teeth, the hysteresis loss density is:

$$p_{hyst}(teeth) = k_{hyst} \cdot B_{st}^{\beta_{St}} \cdot \omega_{el} \quad \text{Equation 4-44}$$

In the stator yoke, the hysteresis loss density is:

$$p_{hyst}(yoke) = k_{hyst} \cdot B_{sy}^{\beta_{St}} \cdot \omega_{el} \quad \text{Equation 4-45}$$

For the eddy current it is convenient to represent the average loss density as a function of the time rate of change of the vector flux density [10]. The instantaneous eddy current loss density can be expressed as

$$p_{eddy} = 2 \cdot k_{eddy} \cdot \left(\frac{dB}{dt} \right)^2 \quad \text{Equation 4-46}$$

Based on FEM-comparisons and taking both radial and circumferential flux components into account, a set of optimised equations for the analytical eddy current loss calculation can be found [9]. The average eddy current loss density in the teeth can then be expressed as

$$p_{eddy}(teeth) = \frac{12}{\pi^2} \cdot q \cdot k_{eddy} \cdot k_q \cdot k_c \cdot (\omega_{el} \cdot B_{st})^2 \quad \text{Equation 4-47}$$

where k_q and k_c are correction factors depending on the geometry which can be found up from Figure 4-9 and Figure 4-10 respectively. It can be seen that the eddy current loss is proportional to the number of slots per pole-phase q . A modified yoke eddy current loss model can be expressed as

$$p_{eddy}(yoke) = \frac{1}{cov} \cdot \frac{8}{\pi^2} \cdot k_{eddy} \cdot (\omega_{el} \cdot B_{sy})^2 \cdot \left(1 + \frac{8 \cdot k_q \cdot h_{sy}^2}{27 \cdot cov \cdot q \cdot \tau_{s2}^2} \right) \quad \text{Equation 4-48}$$

where τ_{s2} is the projected slot pitch at the middle of the yoke. The eddy current loss in the yoke is composed of a contribution of the longitudinal flux component and a contribution of the normal flux component.

Total iron losses are obtained by summing the eddy current losses and hysteresis losses in the teeth and yoke:

$$P_{iron} = (p_{hyst}(teeth) + p_{eddy}(teeth)) \cdot V_t + (p_{hyst}(yoke) + p_{eddy}(yoke)) \cdot V_y \quad \text{Equation 4-49}$$

where V_t and V_y are the volume of stator teeth and stator yoke respectively.

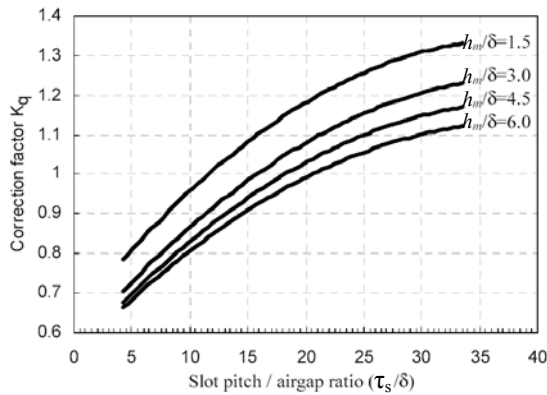


Figure 4-9 Correction factor k_q

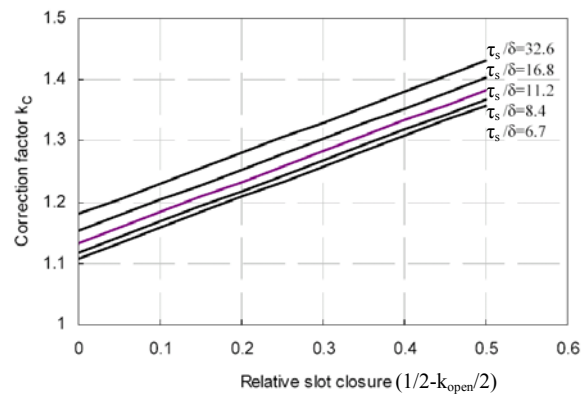


Figure 4-10 Correction factor k_c

Modelling of the iron resistance as described above includes some simplifications and inaccuracies that are discussed subsequently.

- The armature reaction is not considered. The stator current distorts the airgap flux density and has an influence on the prediction of iron losses. More details about the armature reaction can be found in chapter 4.1.4.
- The iron saturation is neglected. However the machine inductance L_m and the induced voltage E vary according to the level of saturation. The variations could be defined as a function of the level of current loading in the d- and q-axis [11].

Some possibilities to reduce the eddy current losses are:

- Thinner laminations or core plates with a high electrical resistivity reduce the eddy current losses.
- Reduce the level of flux density in the stator teeth and yoke (larger dimensions).
- The eddy current losses in the teeth may be several times higher than those of a machine with pure sinusoidal airgap flux density. This is due to the rapid rise of the flux density in the teeth. The magnetisation or the design of the magnet shape can reduce the eddy current losses (refer to App. D).
- The increase of iron losses due to punching, machining and current dependencies amounts to about 50 - 80 % (according to Oberretl [16]) for induction motors. It must be as well considered during the production of PM-motors. The iron lamination is damaged along the edges whereby the permeability is worsened and the iron losses are increased. Glowing of the iron laminations reestablishes the original properties [16].

The efficiency η of the SMPM-motor can be calculated from the output power P_{out} and the total iron and copper losses according to Equation 4-50. As mentioned above, additional losses (friction and stray losses) are not included.

$$\eta = \frac{P_{out}}{P_{out} + P_{cu} + P_{iron}} \quad \text{Equation 4-50}$$

4.1.4 Armature reaction and magnet protection

The actual airgap flux density is not only dependent on the flux produced by the magnets (see Figure 4-11 a) but also on the armature reaction that distorts the airgap flux density. Assuming the stator current produces a sinusoidal flux density, its peak value $B_{\delta,arm}$ in the airgap is:

$$\hat{B}_{\delta,arm} = \mu_0 \cdot \hat{H} = \mu_0 \cdot \frac{N \cdot \hat{I}}{\delta_e + \frac{l_m}{\mu_r}} = \frac{3 \cdot \mu_0}{\pi \cdot \left(\delta_e + \frac{l_m}{\mu_r} \right)} \cdot q \cdot n_s \cdot k_{wl} \cdot \hat{I} \quad \text{Equation 4-51}$$

The relative permeability of iron is assumed as infinite. Equation 4-51 shows that the armature reaction decreases when the effective airgap δ_e increases. Thus, the armature reaction for machines with large airgap such as SMPM-motors is relatively small. The armature reaction will mainly saturate the stator back and therefore should be taken into account when calculating the height of the stator yoke h_{sy} . The additional flux per pole Φ_{ap} produced by the armature current can be calculated as

$$\Phi_{p,arm} = \frac{2}{p} \cdot \hat{B}_{\delta,arm} \cdot \sin\left(\frac{\pi}{2} - \alpha - \gamma\right) \cdot D \cdot l \quad \text{Equation 4-52}$$

where γ is the current angle. Figure 4-11 b) shows the airgap flux density by the stator current at base speed. According to the current angle γ the airgap flux distribution is shifted (compare to Equation 4-52). The iron saturation is neglected. The term from Equation 4-52 has to be considered so that the height of the stator yoke h_{sy} is not underestimated during the analytical calculation.

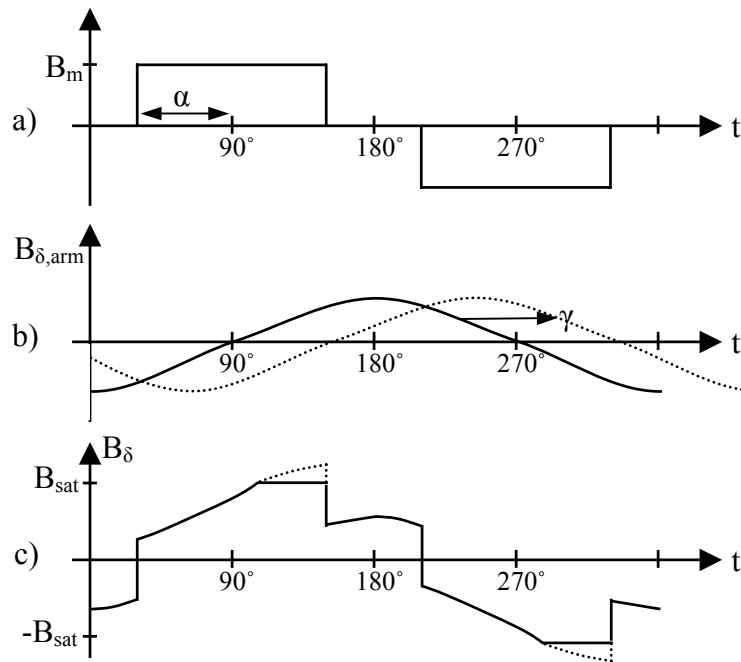


Figure 4-11 Armature reaction
a) Flux density by the magnets
b) Flux density by the stator current (rated conditions, $\gamma=0^\circ$)
c) Resulting airgap flux density

A schematic example of the resulting airgap flux density under load conditions is shown in Figure 4-11 c). The dashed line is the total airgap flux density assuming negligible saturation, while the solid line represents the airgap flux density when the stator teeth saturate at B_{sat} , setting a limit to the peak flux density.

All machines face a risk of a short circuit and most applications require a short time overload capability, leading to a higher current than the rated value. In a PM-machine there is a risk of demagnetisation of the rotor magnets due to the high currents that produce a reverse field. The reverse field should never be allowed to force the magnets beyond the demagnetisation knee (B_D , H_D) on the linear part of the demagnetisation curve (refer to Figure 4-12). The knee is temperature dependent (it moves up in the second quadrant when the temperature increases), thus the demagnetisation curve for the maximum expected temperature of the magnets must be used in the design for their protection. Particularly PM machines must be carefully designed to avoid problems from reversed fields.

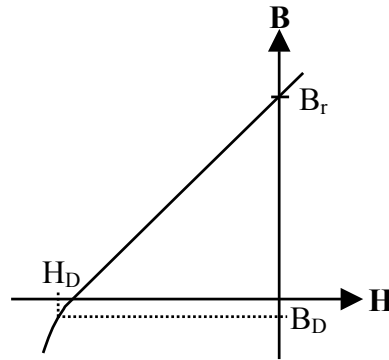


Figure 4-12 Demagnetisation curve for a typical NdFeB magnet

To prevent the risk of demagnetisation, no part of the magnets should be exposed to a flux lower than B_D . The limit for the flux density produced by the stator current will then be

$$\hat{B}_{\delta,arm} \leq B_m - B_D \quad \text{Equation 4-53}$$

and results in a maximum allowable stator current

$$\hat{I}_{\max} \leq \pi \cdot \frac{B_r \cdot l_m - B_D \cdot (l_m + \mu_r \cdot \delta_e)}{3 \cdot \mu_0 \cdot \mu_r \cdot q \cdot n_s \cdot k_{w1}} \quad \text{Equation 4-54}$$

4.2 Parameter study

The stator of the induction motor TSP 112/4-165 that shall be replaced by the SMPM is used for the parameter study. The influence of different parameters as the number of poles or the design of the rotor on the motor characteristics is investigated. Supplementary, a SMPM is optimised for compactness in section 4.2.3.

4.2.1 Dimensions of the basic geometry

As mentioned above, the geometry of the stator is based on the one from the induction motor TSP 112/4-165. One fourth of it is shown in Figure 4-13. The dimensions of the stator are given in Table 4-1.

outer stator diameter D_v	178 mm	stator tooth width b_{ts}	4.8 mm
inner stator diameter D	110 mm	slot wedge height h_{sw}	1.4 mm
height of the stator yoke h_{sy}	13.5 mm	slot opening angle	30°
height of the stator slot h_{ss}	20.5 mm	stator slot area A_{sl}	106 mm ²
number of stator slots Q_s	36	stator slot pitch τ_s	9.6 mm
active machine length l	165 mm	slot opening factor k_{open}	0.57

Table 4-1 Stator dimensions

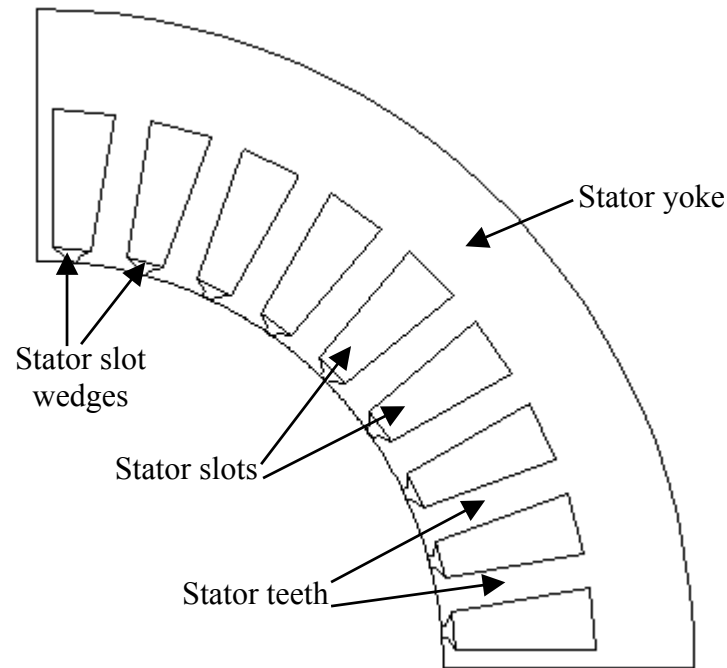


Figure 4-13 Stator of the induction motor TSP 112/4-165

The induction motor is a four-pole machine which means that the number of stator slots per phase and pole (q) is 3. In each slot there are 3 turns. These three turns consist of 12 parallel conductors of 1.32 mm diameter. The stator fill factor f_s can be calculated as 0.465. The stator windings are Y connected and there are 2 parallel coils per phase (one under each pole pair).

It is possible to change the winding in regards of the pole number or the number of turns per stator slot. This is due to the fact that the arrangement of the stator winding is not fixed by the manufacturer but changed according to requirements.

Figure 4-14 shows a possible SMPM rotor. This basic rotor is defined on the dimensions given in Table 4-2. The airgap length δ can be calculated as 1 mm for the given stator and rotor dimensions.

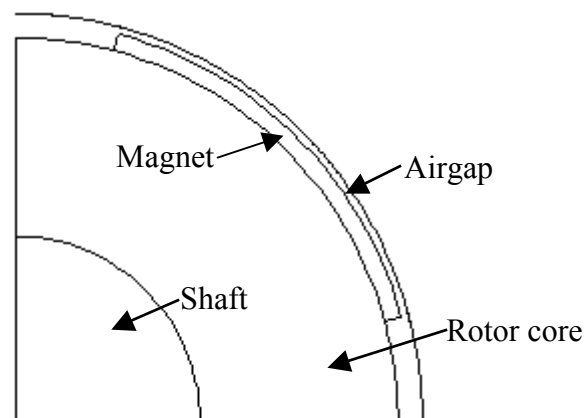


Figure 4-14 Basic SMPM rotor with airgap

airgap length δ	1 mm	magnet thickness h_m	2.5 mm
shaft diameter D_i	50 mm	half pole angle α	60°
rotor core diameter D_{rc}	103 mm	rotor yoke height h_{ry}	26.5 mm

Table 4-2 Rotor dimensions and airgap length

4.2.2 Influence of the number of poles

The choice of the number of poles (p) is discussed in this chapter. From the results, some general reflections concerning the number of poles are presented.

At first, the design with the stator from the induction motor and the basic rotor defined in section 4.2.1 is tested. The number of poles is $p = 4$. The stator current is set to give the demanded operation performance (a rated torque of 60 Nm at a rated speed of 1500 rpm).

It can be seen, that the yoke is saturated ($B_{sy} = 2.05$ T). This causes large iron losses and reduces the efficiency. If the number of poles is increased to $p = 6$, the flux density in the yoke is reasonably reduced ($B_{sy} = 1.27$ T). In return the field-weakening capabilities are reduced (compare to the maximum field weakening speed ω_{max} and the CPSR in Table 4-3).

number of poles p	electrical frequency f	maximum field-weakening speed ω_{max}^*	CPSR [*]	copper loss P_{cu}	no-load iron loss P_{iron}
4	50 Hz	2.85	2.03	332 W	159 W
6	75 Hz	1.88	1.40	295 W	149 W
8 ^{**}	100 Hz	1.61	1.24	283 W	159 W

* The maximum field-weakening speed and the CPSR are calculated without iron losses.

** A two-layer winding is necessary, the number of stator slots per pole per phase q is 1.5.

Table 4-3 Effect of the pole number on the field-weakening capability and the losses

In general, the number of poles should be decreased with increasing maximum speed to limit the commutation frequency (refer to the electrical frequency in Table 4-3). This avoids excessive switching losses in the transistors and iron losses in the stator. Another good reason to decrease the number of poles is the fact that the stator ampere-conductors per pole decrease in inverse proportion. Thus the per-unit inductance and synchronous reactance decrease in motors of higher pole-number allowing a smaller field-weakening range. This can be seen in Table 4-3, where the CPSR is reduced from 2.03 for a four pole design to 1.40 for a six pole design.

The advantage of a large number of poles is not only a smooth torque. An increase of the number of poles also reduces the required thickness of the rotor and stator yoke and allows a more compact design. In addition, the length of the end turns is decreased with an increasing number of poles. Consequently, the copper losses are reduced (compare with Table 4-3). The no-load iron losses P_{iron} for different pole numbers are more or less

constant, as the increasing frequency is compensated with a reduced level of flux density (refer to section 4.1.3 for more details).

4.2.3 Compact design

In the previous chapter, it is shown that a high pole number allows compact designs. But in return, the switching and iron losses increase with an increasing pole number. Therefore, a 4-pole design that combines both compactness and low losses is presented in this section. The outer rotor diameter D_y and the active machine length l are reduced by 8 and 5 mm respectively compared to the outer dimensions of the induction motor stator. One quarter of the compact SMPM machine is shown in Figure 4-15. The machine parameters are given in Table 4-4.

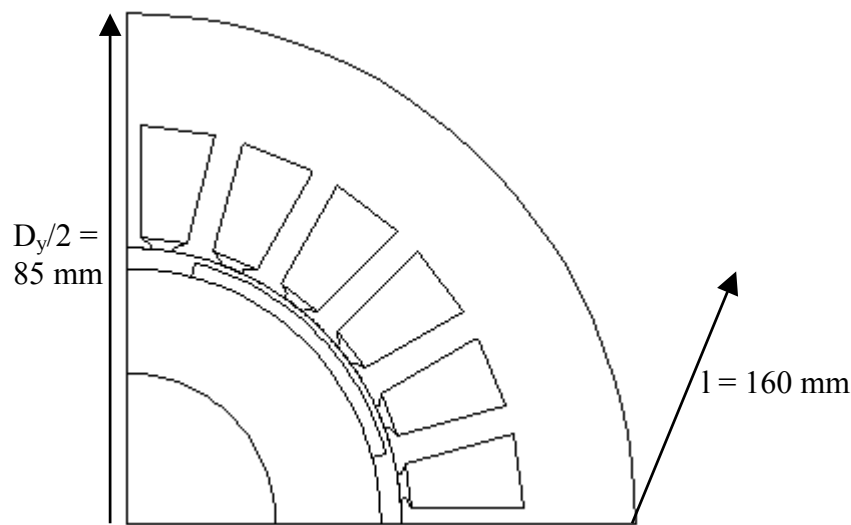


Figure 4-15 Geometry of the compact design

outer stator diameter D_y	170 mm	stator tooth width b_{ts}	4.8 mm
inner stator diameter D	91.8 mm	slot wedge height h_{sw}	1.4 mm
height of the stator yoke h_{sy}	18.6 mm	slot opening angle	30°
height of the stator slot h_{ss}	20.5 mm	stator slot area A_{sl}	188 mm ²
number of stator slots Q_s	24	stator slot pitch τ_s	11.9 mm
active machine length l	160 mm	slot opening factor k_{open}	0.57
airgap length δ	1 mm	magnet thickness h_m	2.4 mm
shaft diameter D_i	50 mm	half pole angle α	60°
rotor core diameter D_{rc}	85 mm	rotor yoke height h_{ry}	17.5 mm

Table 4-4 Dimensions of the compact design

Table 4-5 shows that the analytical values for the flux densities at different points are within the limit values. This proves that the magnetic design is reasonable. The current density and the peak values of the base voltage and the stator current are within the limit values as well.

	analytical	limit value
fundamental airgap flux density	0.80 T	~0.90 T
maximum flux density in the stator teeth	1.78 T	~1.80 T
maximum flux density in the stator yoke	1.29 T	~1.40 T
maximum flux density in the rotor yoke	0.97 T	~1.40 T
peak value of the base voltage	27.7 V	< 28.6 V
peak value of the stator current	304.7 A	< 461.3 A*
current density	6.9 A/mm ²	< 7 A/mm ²

*The limiting value for the stator current is given from the protection of the magnets against demagnetisation (refer to Equation 4-54).

Table 4-5 Analytical and limit values for the flux densities and the base voltage and current

Figure 4-16 shows the power against speed curve. The field-weakening range without iron losses is 6.1 times the base speed, the CPSR is 4.2. The iron losses are as well included and a second power against speed curve including them is shown. The iron losses are calculated using the improved iron loss model from section 5.3. It can be seen, that the iron losses only slightly affect the field-weakening capabilities. The field-weakening range and CPSR with iron losses are the same, but the output power and torque are reduced by 1 % (torque of 59.4 Nm with iron losses compared to 60 Nm without).

The power factor $\cos(\varphi)$ at base speed is 0.80. The efficiency η of the motor including the iron losses is 94.1 %. The efficiency of the induction motor is 84 % at 1375 rpm and 60 Nm.

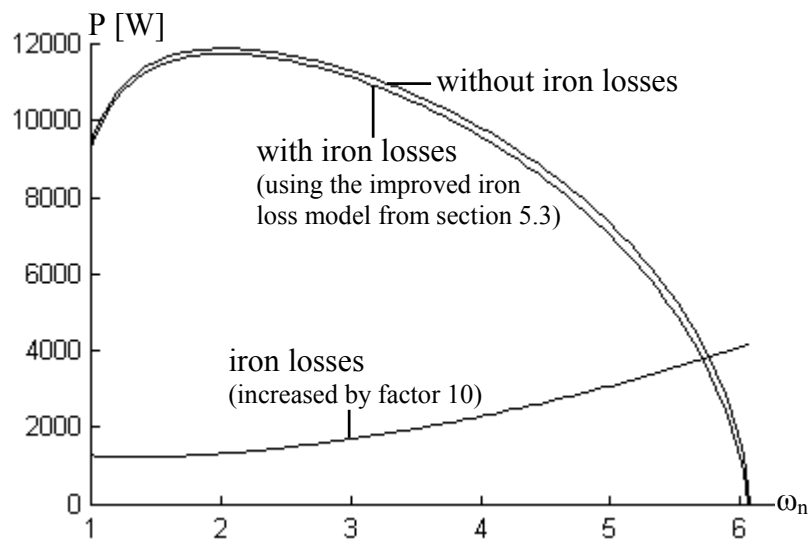


Figure 4-16 Iron losses and power against speed curve

4.2.4 Variations on the rotor geometry

Some studies on the influence of the rotor geometry on the SMPM performance are done in this section. The magnetising inductance L_m , the maximum field-weakening speed ω_{max} , the CPSR, the power factor $\cos(\varphi)$ and the efficiency η are looked at.

These parameter variations base on the compact 4-pole design presented in the previous section. In the following three tables, this base design is highlighted.

A first parameter variation is done for a different magnet thickness l_m . The airgap length δ and the inner stator diameter D are chosen constant as 1 mm and 91.8 mm respectively. The results are shown in Table 4-6.

magnet thickness l_m	2.3 mm	2.4 mm	2.5 mm	2.6 mm	2.7 mm
rotor core diameter d_{rc}	85.2 mm	85 mm	84.8 mm	84.6 mm	84.4 mm
magn. inductance L_m	174 nH	169 nH	164 nH	160 nH	156 nH
max. fw range ω_{max}	7.8	6.1	5.0	4.3	3.8
CPSR	5.4	4.2	3.5	3.0	2.7
power factor $\cos(\varphi)$	0.79	0.80	0.82	0.83	0.84
efficiency η^* at ω_b	94.0%	94.1%	94.3%	94.4%	94.5%

*The efficiency η is calculated from the no-load iron losses at rated speed.

Table 4-6 Influence of the magnet thickness

A second parameter variation is done for a constant effective airgap. The rotor core diameter d_{rc} is fixed to 85 mm and the inner stator diameter D is fixed to 91.8 mm. The airgap length δ and the magnet thickness l_m are varied. The results are shown in Table 4-7.

airgap length δ	0.7 mm	0.8 mm	0.9 mm	1 mm	1.1 mm
magnet thickness l_m	2.7 mm	2.6 mm	2.5 mm	2.4 mm	2.3 mm
magn. inductance L_m	171 nH	170 nH	170 nH	169 nH	168 nH
max. fw range ω_{max}	3.1	3.7	4.5	6.1	9.5
CPSR	2.2	2.6	3.1	4.2	6.6
power facto $\cos(\varphi)$	0.86	0.84	0.82	0.80	0.78
efficiency η^* at ω_b	95.1%	94.8%	94.5%	94.1%	93.7%

*The efficiency η is calculated from the no-load iron losses at rated speed.

Table 4-7 Parameter variations with constant effective airgap

A third parameter variation is done for a constant magnet thickness $l_m = 2.4$ mm. The stator is as well fixed to an inner stator diameter of $D = 91.8$ mm. The influence of a varying airgap length δ is shown in Table 4-8.

airgap length δ	0.7 mm	0.8 mm	0.9 mm	1 mm	1.1 mm
rotor core diameter d_{rc}	85.6 mm	85.4 mm	85.2 mm	85 mm	84.8 mm
magn. inductance L_m	187 nH	180 nH	174 nH	169 nH	164 nH
max. fw range ω_{max}	4.3	4.8	5.3	6.1	7.0
CPSR	3	3.3	3.7	4.2	4.8
power facto $\cos(\varphi)$	0.83	0.82	0.81	0.80	0.79
efficiency η^* at ω_b	94.9%	94.6%	94.4%	94.1%	93.9%

*The efficiency η is calculated from the no-load iron losses at rated speed.

Table 4-8 Influence of the airgap length

The conclusions of this parameter variations is, that an optimisation in regard to good efficiency η and power factor $\cos(\varphi)$ is always at the expense of a lower field-weakening and constant power speed range. But a good design has a small airgap δ and effective airgap δ_e (compare to section 4.1).

5 Verification with FEM

5.1 Setup of the Flux2D-Simulation

This section introduces some specific knowledge about Flux2D and the setup of the simulations. It is based on the Flux2D tutorial about the "Brushless Permanent Magnet Motor" [12]. However, this section is not entitled to give a complete introduction to Flux2D.

5.1.1 Constructing the geometry and the mesh

The geometry shown in Figure 5-1 is completely parametrised using 13 relevant parameters (see Table 5-1). Defining parameters simplifies the geometry design and supports later modifications. Because of the motor's periodicities, only 1/4 (1 pole) of the machine is required for the modelling. Our model consists of 6 stator slots (MA, PB, MC, PA, refer to section 5.1.3 for details) and 1 north magnet pole.

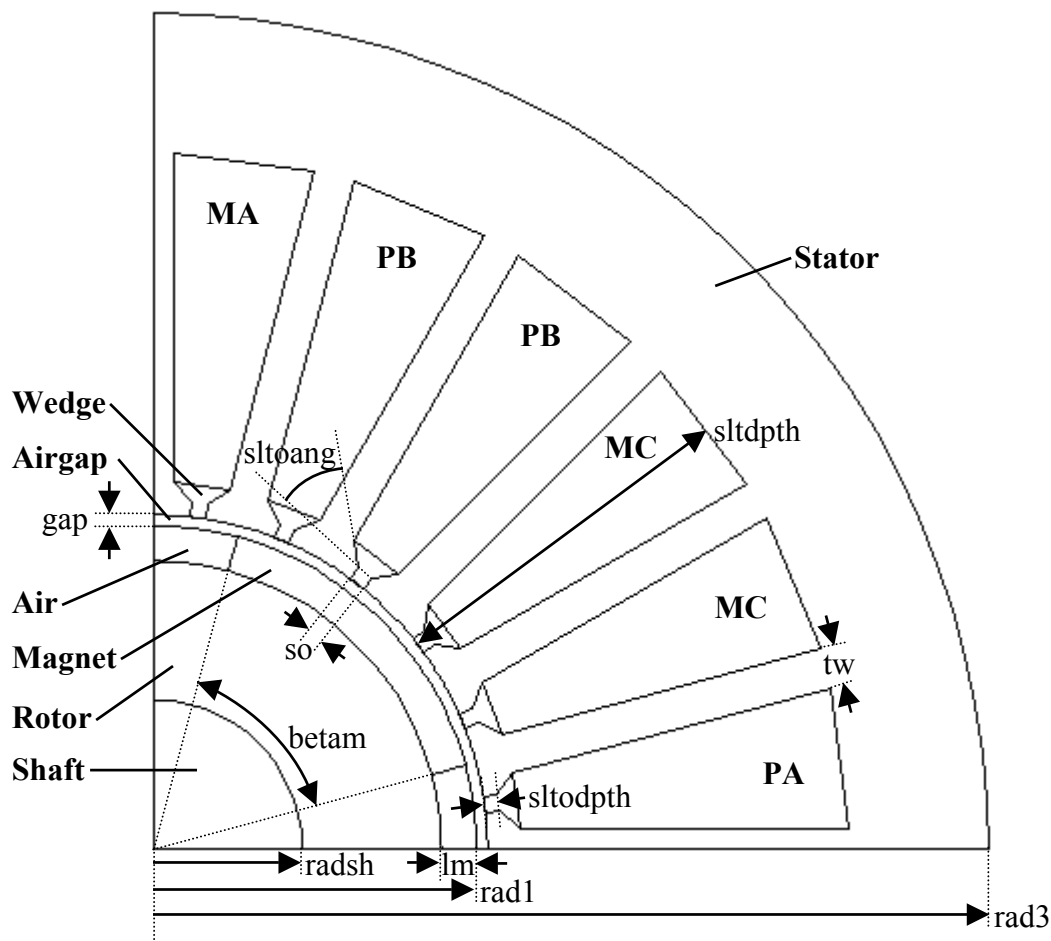


Figure 5-1 Geometry with relevant parameters

Table 5-1 shows the Flux2D parameters, their relation to the symbols used in this report and their values.

Flux2D	Report	Value
npoles	p	4
radsh	$D_i/2$	13.38 mm
rad1	$D_{rc}/2+l_m$	29 mm
gap	δ	1 mm
lm	l_m	3.14 mm
betam	$2 \cdot \alpha$	120°
rad3	$D_v/2$	75 mm
nslots	Q_s	24
tw	b_{ts}	3.62 mm
sltdpth	h_{ss}	32.52 mm
so	$k_{open} \cdot b_{ss1}$	1.43 mm
sltodpth	$h_{sw}/2$	1.25 mm
sltoang	$\sin^{-1} \left(\frac{h_{sw}}{b_{ss1} \cdot (1 - k_{open})} \right)$	43.18°

Table 5-1 Geometry parameters

Whenever a mesh is generated, it is important to consider the requirements of the different regions. A fine mesh in the regions around the airgap is required:

- The part of the rotor nearest to the airgap (including the magnet).
- The stator teeth: The teeth present a possible region of saturation due to the high flux density in the area.
- The airgap: A fine mesh in and around the airgap will produce higher accuracy on the force and torque computation.

The automatic mesh generator usually produces an adequate mesh in terms of quality, accuracy and size. However it is better to adjust and control the density of the mesh with a specific mesh generator.

5.1.2 Description of the materials

The materials used to define the physical properties of the different problems analyzed by FLUX2D are stored in the materials database (MATERI.DAT file). In this section, the properties of the magnet and iron lamination material are shown.

Flux2D features a linear model of magnets, characterised by a constant value of the relative permeability μ_r and a constant value of the remanence flux density B_r . The specific values can be found in Figure 5-2.

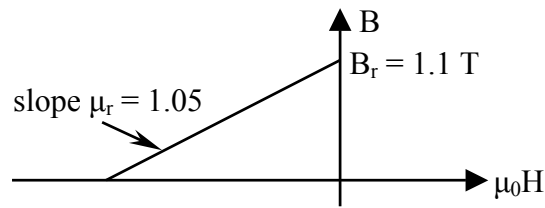


Figure 5-2 Definition of the linear magnet material

The non-linear iron lamination material is defined by a model called "Analytic saturation curve with bend adjustment". The data required for the B(H) curve are the saturation magnetization B_{sat} and the initial relative permeability μ_r . The addition of the coefficient a allows a better control of the curve bend. Consequently, the model and the curve from the datasheet of the lamination manufacturer can get closer to each other. Figure 5-3 shows the B(H) curve (the crosses represent values from the datasheet) and the values of the chosen parameters. Adjusting the curve to the real properties is rather difficult, e.g. it's not possible to include the lower bend of the B(H) curve. But as the motor is operating at saturation condition, the first bend of the B(H) curve can be neglected.

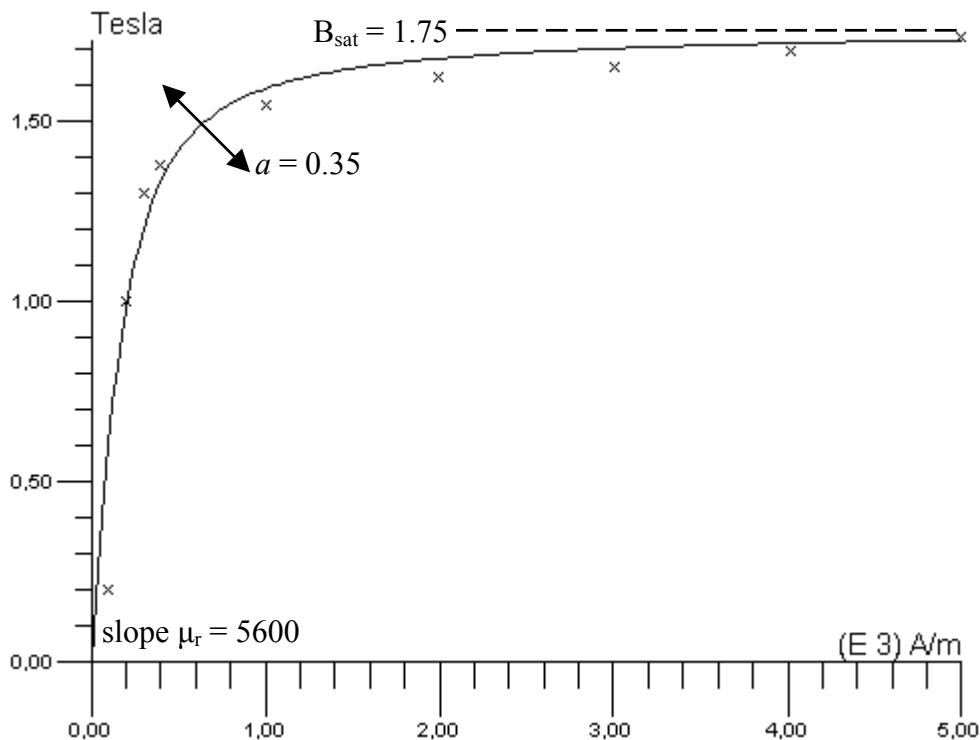


Figure 5-3 B(H) curve of the iron lamination M800-65A

To compute the iron losses in a region, some coefficients need to be supplied. The iron loss coefficients of the used iron lamination M800-65A can be calculated from the properties given by the distributor. The lamination sheet thickness (d_{lam}) is given as 0.65 mm. For a given iron resistivity of $\rho_{\text{iron}} = 25 \mu\Omega\text{cm}$, the iron conductivity σ_{iron} can be calculated as

$$\sigma_{iron} = \frac{1}{\rho_{iron}} = 4e6 (\Omega m)^{-1} \quad \text{Equation 5-1}$$

The hysteresis loss coefficient $k_{hyst}(FEM)^{14}$ and the excess loss coefficient k_{exc} can be determined referring to the information supplied by the lamination manufacturers. In general they provide the iron losses for a given flux density and a given frequency. The specific total loss for the iron lamination M800-65A at 50 Hz and for flux densities between 0.9 and 1.6 T is given in Table 5-2. The iron loss is given in W/kg and W/m³, which differ by the conventional iron lamination density of 7800 kg/m³.

B [T]	0.90	1.00	1.10	1.20	1.30	1.40	1.50	1.60
P _{iron} [W/kg]	2.58	3.09	3.67	4.32	5.08	5.94	6.90	7.93
P _{iron} [W/m ³]	20124	24102	28626	33696	39624	46332	53820	61854

Table 5-2 Specific total loss of iron lamination M800-65A at 50 Hz

Two values are required to determine the coefficients $k_{hyst}(FEM)$ and k_{exc} using Equation 5-2 below. This equation describes how the total losses are calculated in a magnetic region during the analysis in Flux2D. The losses include the hysteresis losses, the eddy current losses and the excess losses:

$$P_{iron} = k_{hyst}(FEM) \cdot B^2 \cdot f + \pi^2 \cdot \frac{\sigma_{iron} \cdot d_{lam}^2}{6} \cdot B^2 \cdot f^2 + k_{exc} \cdot (B \cdot f)^{3/2} \cdot 8.67 \quad \text{Equation 5-2}$$

For the specific total losses at 0.9 and 1.5 T from Table 5-2, the hysteresis loss coefficient can be calculated as $k_{hyst}(FEM) = 279.81 \text{ W}\cdot\text{s}/\text{T}^2/\text{m}^3$ and the excess loss coefficient as $k_{exc} = 1.28 \text{ W}\cdot(\text{s}/\text{T})^{3/2}/\text{m}^3$. These coefficients may slightly differ for the calculation with two different flux densities. Equation 5-3 and Equation 5-4 show the correlation between the loss coefficients used in the report (k_{hyst} and k_{eddy}) and the ones used in Flux2D ($k_{hyst}(FEM)$, σ_{iron} and d_{lam}). Table 5-5 includes all loss coefficient used for the FEM simulations.

$$k_{hyst} = \frac{k_{hyst}(FEM)}{2\pi} \quad \text{Equation 5-3}$$

$$k_{eddy} = \frac{\sigma_{iron} \cdot d_{lam}^2}{24} \quad \text{Equation 5-4}$$

5.1.3 Electrical circuits and description of the physical properties

The computation of the induced voltage or the definition of the stator currents is done by connecting the windings to an external electric circuit. Figure 5-4 a) shows an electrical circuit for no-load simulations. It shows 2 coils of the phase A (PA and MA) and 1 coil

¹⁴ The hysteresis coefficient for the calculation of the hysteresis losses in Flux2D is defined differently than introduced in this report. So it is referred to as $k_{hyst}(FEM)$. Equation 5-3 shows the correlation between them.

for phase B and phase C (PB and MC respectively). The three resistors R build a symmetric three-phase resistance.

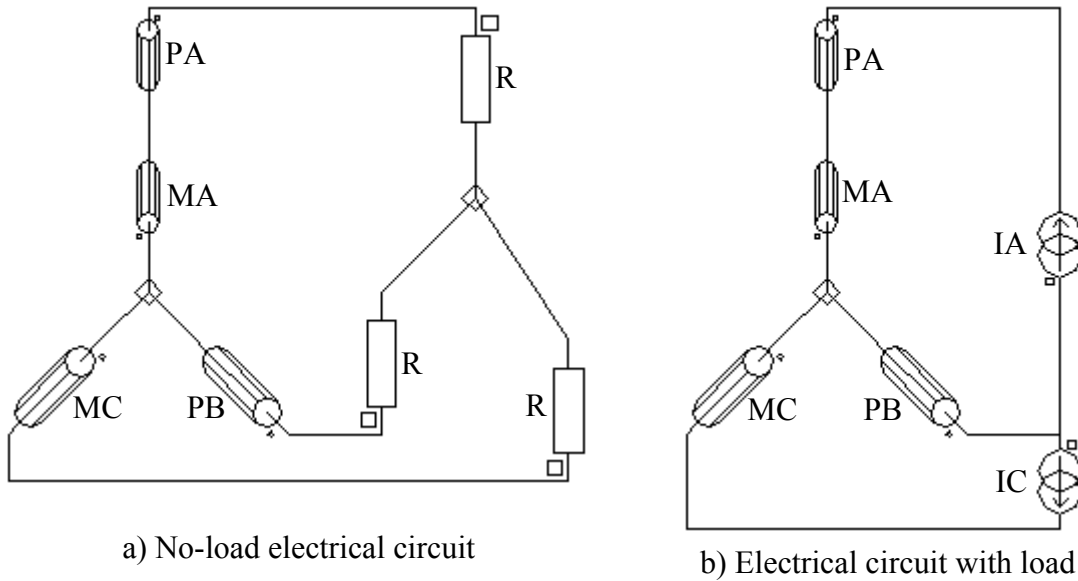


Figure 5-4 Constructing the electrical circuits

Figure 5-4 b) shows an electrical circuit for load simulations. The two current sources represent a star shaped three-phase current source. In Flux2D it cannot be modelled classically because an electric mesh must have only one current source. This problem can be overcome by removing one current source. This allows the imposition of the correct currents. The current source is always orientated: the current leaves by its hot point (represented by the square) when the value of the current is positive [12].

After the definition of the electrical circuit, the physical properties are assigned. The depth of the object (length l) and the materials are assigned to the regions and the boundary conditions are defined. Then the physical properties for the circuit are set (see Table 5-3).

PA	$n_s = 5$	$R_{cu} = 0.921e-3 \Omega$	
MA	$n_s = 5$	$R_{cu} = 0.921e-3 \Omega$	
MC	$n_s = 10$	$R_{cu} = 1.841e-3 \Omega$	
PB	$n_s = 10$	$R_{cu} = 1.841e-3 \Omega$	
R	10000Ω		
IA	$\hat{I} = 196.93 \text{ A}$	$f = 50 \text{ Hz (at rated speed)}$	$\text{phase}^* = 0^\circ + \gamma$
IC	$\hat{I} = 196.93 \text{ A}$	$f = 50 \text{ Hz (at rated speed)}$	$\text{phase}^* = 120^\circ + \gamma$

* A current angle $\gamma = 0^\circ$ indicates pure q-axis current. On the contrary, a current angle $\gamma = 90^\circ$ indicates pure negative d-axis current.

Table 5-3 Physical properties of the circuit components

The coils PA and MA each represent one slot of the positive and negative phase A and contain 5 conductors. The phase resistance is calculated from the phase resistance value ($R_{cu} = 7.365 \text{ m}\Omega/\text{phase}$). It must be divided by the pole-number to receive the winding

resistance per phase and per pole ($R_{cu} = 1.84 \text{ m}\Omega/\text{phase/pole}$). But as PA and MA only represent half of the complete coil, another division by 2 is necessary to obtain $0.921 \text{ m}\Omega$. Each of MC and PB represents two slots. The number of turns for them is twice the value for one slot ($n_s = 10$). Their resistance is also twice the resistance for one slot ($R_{cu} = 1.841 \text{ m}\Omega$).

5.1.4 Solving processor

It is important to choose a sufficient number of time steps over one electrical period. For this problem, 48 time steps are chosen over one electrical period (180 degrees) to make 4 time steps per slot pitch or 1 time step every 3.75 degrees (180/48). The time step is computed as follows: For each time step the rotor will rotate 3.75 degrees at 1500 rpm ¹⁵ (at rated speed). The time step is then $3.75/1500/6 = 0.417 \text{ ms}$.

5.2 Results

The simulations were conducted on a motor with the parameters described in Table 5-1. The setup of the simulations is described in section 5.1.

5.2.1 No-load simulation

The no-load simulation is implemented to check the distribution of the airgap flux, the induced voltage E and the no-load iron losses. Comparisons to the expected values allow conclusions of the accuracy of the analytical model.

¹⁵ The speed is calculated as $2/p \cdot f \cdot 60$

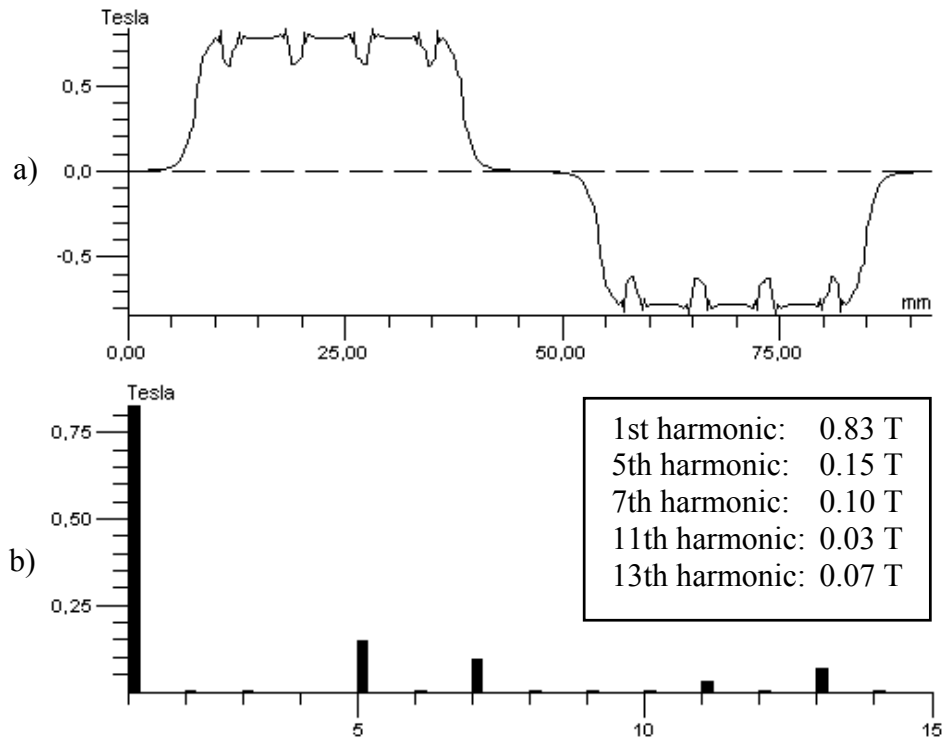


Figure 5-5 Airgap flux distribution (a) and respective spectrum (b)

The airgap flux density of half the motor and the respective spectrum analysis are shown in Figure 5-5. In addition to the maximum average flux above the magnets B_m and the fundamental component of the airgap flux B_δ , the maximum flux density in the stator teeth B_{st} and yoke B_{sy} have been compared to the expected design values. The results are summarised in Table 5-4.

	analytical values	FEM values
B_m	0.816 T	~ 0.78 T (-4.4%)
\hat{B}_δ	0.9 T	0.83 T (-7.8%)
B_{st}	1.8 T	1.6 T (-11.1%)
B_{sy}	1.05 T	0.96 T (-8.6%)

Table 5-4 Comparison of analytical and FEM flux densities

The reason for the lower airgap flux density values of the FEM simulation is the rotor flux leakage and the influence of the stator slotting, which are not yet considered. A constant for the rotor leakage (k_{leak}) is defined previously in Equation 4-6, but it is not used for the analytical calculation due to the fact that the dependencies of this factor on the geometry are not known. The maximum flux densities in the stator teeth and yoke are also lower than the analytical values. A look at the spectrum of the airgap flux shows that the 3rd harmonic is almost completely suppressed (3rd harmonic: 0.0016 T). The reason is the choice of the half pole angle $\alpha = \pi/3$, that eliminates the 3rd harmonic. Hence for the iron losses, it is a good choice to suppress the low order harmonics as much as possible.

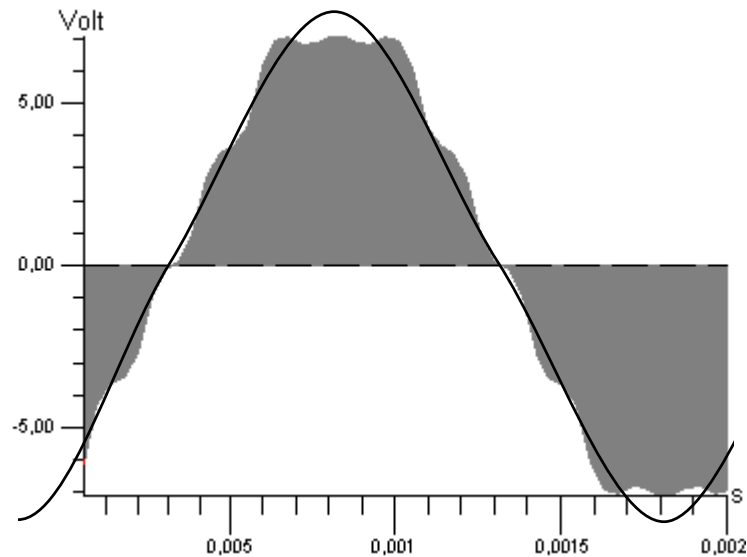


Figure 5-6 Induced voltage E with first harmonic

In Figure 5-6 the induced voltage E with the first harmonic is shown. The value of the first harmonic from the FEM simulation is 7.32 V. As the simulation is only one quarter of the machine, the first harmonic of the induced voltage is four times the measured value, see Table 5-5. A comparison with the expected analytical value shows that the simulated value is 9% smaller (due to the stator leakage). Table 5-5 shows also the iron loss coefficients used for the FEM simulations and a resulting no-load iron loss P_{iron} at base speed of 79.9 W. The difference between the FEM and the analytical value can be explained by the fact, that the flux levels in the stator teeth and yoke are lower than expected (see Table 5-4).

	analytical values	FEM values
induced voltage E	32.2 V	29.3 V (-9.1%)
iron losses P_{iron}	85.6 W	79.9 W (-6.6%)
hysteresis loss coefficient k_{hyst}		280 W·s/T ² /m ³
iron conductivity σ_{iron}		4'000'000 $\Omega^{-1}\text{m}^{-1}$
excess loss coefficient k_{exc}		1.25 W·(s/T) ^{3/2} /m ³
lamination sheet thickness d_{lam}		0.00065 m
lamination stacking factor k_i		1
electrical frequency f (at rated speed)		50 Hz

Table 5-5 Induced voltage and iron losses

5.2.2 Operation at rated speed

At rated speed, the base current is put on the q-axis to obtain the maximal torque-to-current ratio (compare to chapter 3.1.1). The q-axis current I_q is set as 196.93 A (calculated from the analytical model), the d-axis current I_d is zero. Figure 5-7 shows the resultant airgap flux waveform of half the rotor at rated speed.

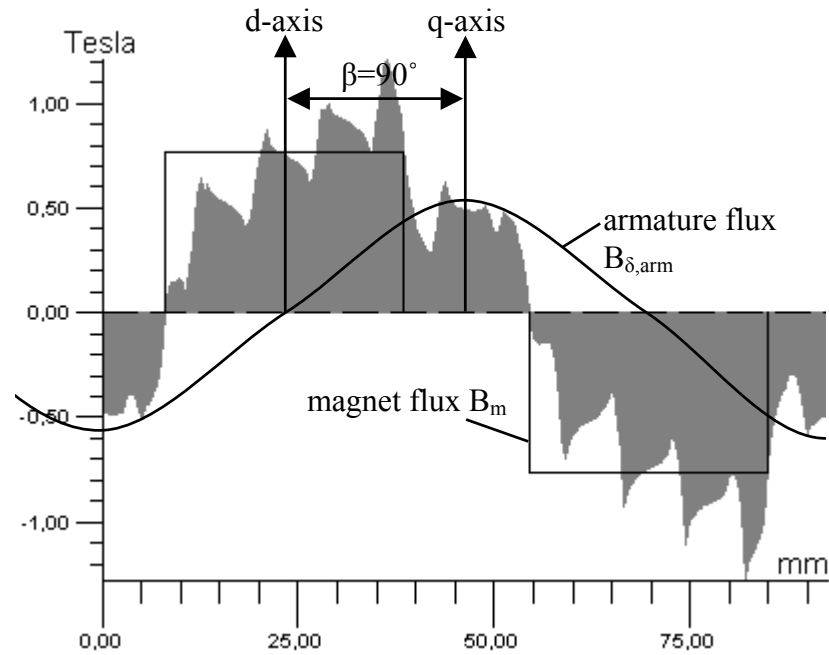


Figure 5-7 Airgap flux of half the rotor at rated speed

The constitution of the airgap flux is shown in Figure 5-7. The idealised magnet flux B_m (according to Equation 4-1) and the idealised armature flux $B_{\delta,arm}$ (according to Equation 4-51) are pictured. The position of the magnet flux in the d-axis and the armature flux in the q-axis can be seen.

Figure 5-8 shows the airgap flux produced by the stator current alone. The influence of the stator slotting (the 12 slots in half the motor can be found in the waveform of Figure 5-8) is massive and leads to distortions. The amplitude of the first harmonic of the airgap flux is 0.5 T (comparing to an analytically calculated value of $\hat{B}_{\delta,arm} = 0.56$ T). The reason of this difference is the stator leakage.

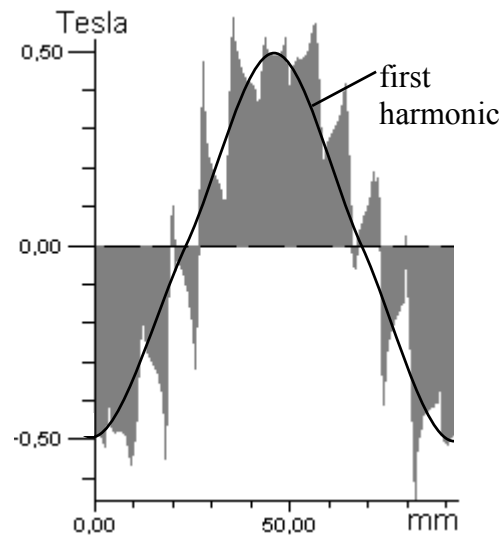


Figure 5-8 Airgap flux produced by the stator current

Table 5-6 shows the comparisons of some expected analytical values and the FEM values. The simulated maximum flux densities in the stator teeth and yoke correspond well to the expected values. The total iron loss P_{iron} is 115.9 W. Table 5-7 shows an itemisation of the different losses (eddy current, hysteresis and excess losses) in the different parts of the machine (stator teeth, stator yoke and rotor yoke). Comparing to the no-load losses (see Table 5-5), the iron losses at rated speed are increased by 45 %.

	analytical values	FEM value
flux density in the stator teeth B_{st}	1.8 T	1.77 T (-1.7%)
flux density in the stator yoke B_{sv}	1.4 T	1.39 T (-0.7%)
torque T	60 Nm	48.15 Nm (-19.8%)
inductance L	0.396 mH*	0.375 mH (-5.3%)
iron losses P_{iron}		115.9 W

* the analytic value of the inductance is composed of two parts: magnetising inductance ($L_m = 0.327$ mH) and stator leakage inductance ($L_{\text{leak}} = 0.069$ mH).

Table 5-6 Comparison of analytical and FEM quantities

area	eddy cur. loss	hysteresis loss	excess loss	total loss
stator teeth	26.0 W	25.3 W	7.6 W	58.9
stator yoke	18.7 W	27.0 W	7.6 W	53.3
rotor yoke	0.03 W	3.6 W	0.04 W	3.7
total iron losses P_{iron}				115.9 W

Table 5-7 Itemisation of the losses from FEM

The torque T from the FEM simulation is 48.15 Nm, nearly 20 % lower than expected. The reason is that the stator leakage flux is not considered when the stator current loading S_1 is analytically calculated. Equation 4-17 shows the proportionality between

the torque T and the stator current loading S_1 . A correction factor is introduced in the expression of the torque to take into account the leakage.

$$T \sim S_1 \rightarrow S_1 \cdot \frac{L_m}{L_m + L_{leak}} = S_1 \cdot 0.826 \quad \text{Equation 5-5}$$

The analytical torque value that we can expect for our chosen geometry including the effect of the stator leakage flux is calculated to 49.55 Nm (compared to 60 Nm without including the stator leakage flux). That is 2.9 % higher than the simulated value and within reasonable limits.

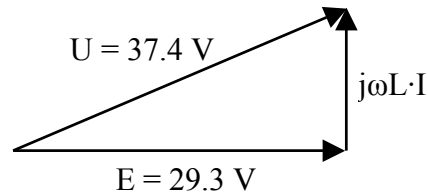


Figure 5-9 Calculation of the motor inductance

The inductance L (consisting of the magnetising inductance L_m and leakage inductance L_{leak}) is more difficult to obtain from the FEM simulations. The Flux2D algorithm to determine the inductance produces unreliable results. Therefore the inductance was calculated from the induced voltage E and the voltage U according to Figure 5-9. The analytical expression is given in Equation 5-8.

$$L = \frac{\sqrt{U^2 - E^2}}{\omega \cdot I} \quad \text{Equation 5-6}$$

5.2.3 Field-weakening operation

In this section, the FEM iron losses and the torque during field-weakening operation are analysed.

For the calculation of the maximum speed and the optimised current angle γ , the normalised magnet flux Ψ_{mn} and inductance L_n of the motor are required (according to chapter 3.2). The base voltage U_b is given as 37.37 V, the current at base speed I as 196.93 A and the base angular frequency ω_b as 314.16 rad/s. Based on Equation 5-7 in section 3.1, the normalised magnet flux can then be calculated as:

$$\Psi_{mn} = \frac{\Psi_m}{\Psi_b} = \frac{E/\omega_b}{U_b/\omega_b} = \frac{93.26 \text{ mWb}}{118.95 \text{ mWb}} = 0.784 \quad \text{Equation 5-7}$$

Similarly, the normalised inductance L_n and normalised maximum speed ω_{max} can be calculated as 0.487 and 6.127 by applying Equation 3-10 and Equation 3-14 respectively.

ω_n	1	2.282	3.563	4.845	6.127
f	50 Hz	114.08 Hz	178.17 Hz	242.25 Hz	306.34 Hz
γ	0°	56.10°	71.17°	79.61°	90°
I_q	196.93 A	109.83 A	63.57 A	35.51 A	0 A
I_d	0 A	-163.46 A	-186.39 A	-193.70 A	-196.93 A
P_{iron}	116 W	166.5 W	258.5 W	363.5 W	511 W
T	48.15 Nm	30.98 Nm	18.01 Nm	10.08 Nm	0.02 Nm

Table 5-8 Field-weakening properties

Four simulations at different speeds are analysed. These four normalised speeds and their corresponding electrical frequencies are shown in Table 5-8. The simulation at base speed ($\omega_n = 1$) is also included in the table. The optimised current angle γ can be calculated based on Equation 3-12. The q- and d-axis currents I_q and I_d can be found from the base current I_b and the current angle γ as in Equation 5-8 and Equation 5-9.

$$I_q = I_b \cdot \cos(\gamma) \quad \text{Equation 5-8}$$

$$I_d = -I_b \cdot \sin(\gamma) \quad \text{Equation 5-9}$$

A diagram of the iron losses P_{iron} at the five different frequencies from the FEM simulation is shown in Figure 5-10. The iron losses increase with increasing demagnetising current although the flux levels are reduced (field-weakening). The iron losses at maximum speed are 4.5 times higher than at base speed (see Table 5-8).

A comparison with the analytically calculated iron losses (see Figure 5-10) shows that the model based on the no-load losses (refer to chapter 4.1.3) is not accurate enough to describe the effects for field-weakening. That is the reason why a more advanced analytical iron loss model is derived in the following section.

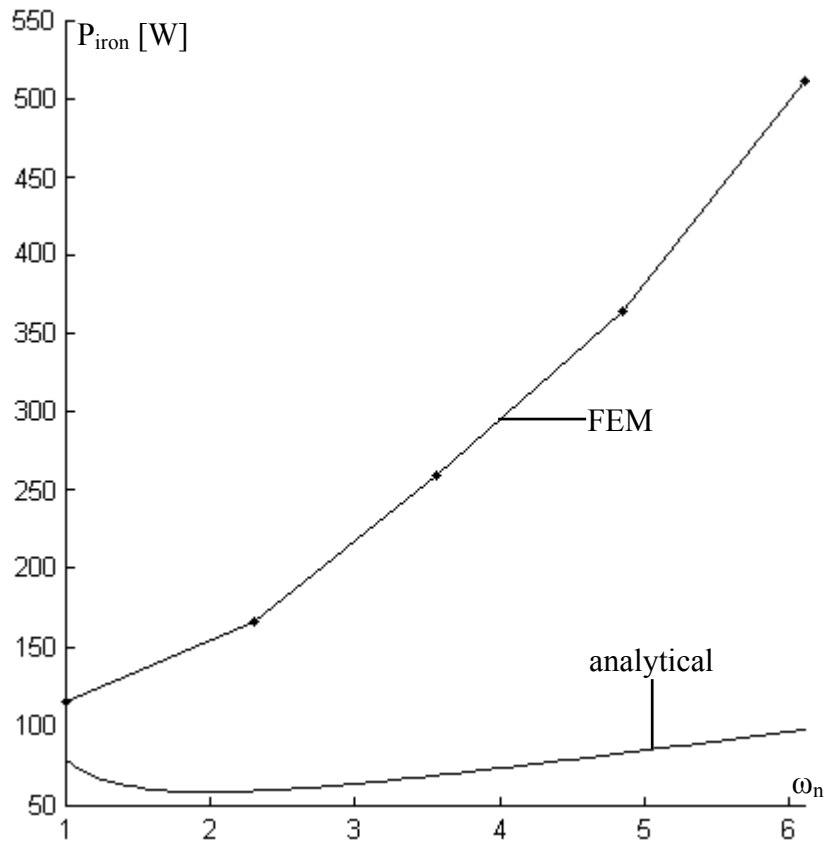


Figure 5-10 Analytical and FEM simulated iron losses

The torque at the five different frequencies is shown in Figure 5-11. As expected, the torque is decreasing with increasing frequency and is getting zero for the maximum speed.

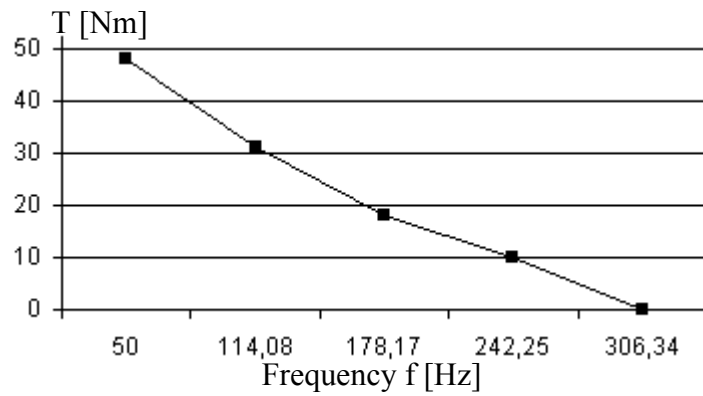


Figure 5-11 FEM torque curve for field-weakening

5.3 Improved analytical iron loss model

From the FEM simulations, the flux distributions in each point of the machine at different speeds are known. In this section, an improved iron loss model that takes the armature reaction into account is developed. The approach is to describe the flux distribution in the stator teeth and yoke. The losses are calculated based on the model of the flux distribution.

The following reflections are general and not fixed to a certain design. But all curves and verifications are based on the design that is described earlier in this chapter at a speed of 178.17 Hz (compare to Table 5-8).

5.3.1 Losses in the stator teeth

The flux distribution in the middle of the stator teeth on half the height is shown in Figure 5-12. Comparing to the flux distribution in the airgap (see Figure 5-7), the flux distribution in the teeth is much smoother and the effect of slotting is not present. The constitution of the resulting flux distribution from the magnet and the stator current can be noticed again.

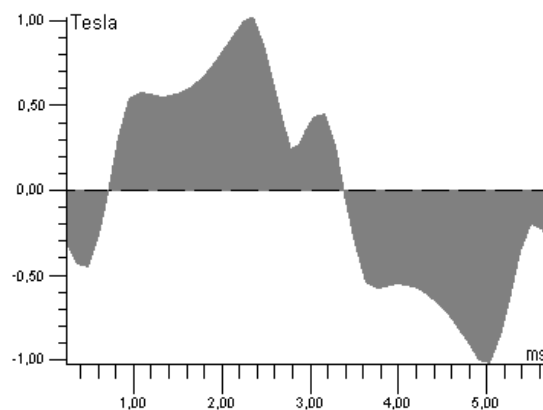


Figure 5-12 Flux distribution in the stator teeth

Our model is based on the fact that the flux in the teeth is the superposition of the flux produced by the magnets and the stator current and can be obtained from the airgap flux. Figure 5-13 shows the airgap flux by the magnets (a) and the stator current (b). The magnet flux is assumed to be trapezoidal. The height of the magnet flux atop of the magnet is B_m and the edge is given by the pole angle 2α and the stator slot pitch τ_s . The airgap flux by the stator current is sinusoidal and the peak value is $\hat{B}_{\delta,arm}$ (Equation 4-34). This sinusoidal waveform is shifted according to the d- and q-components of the stator current.

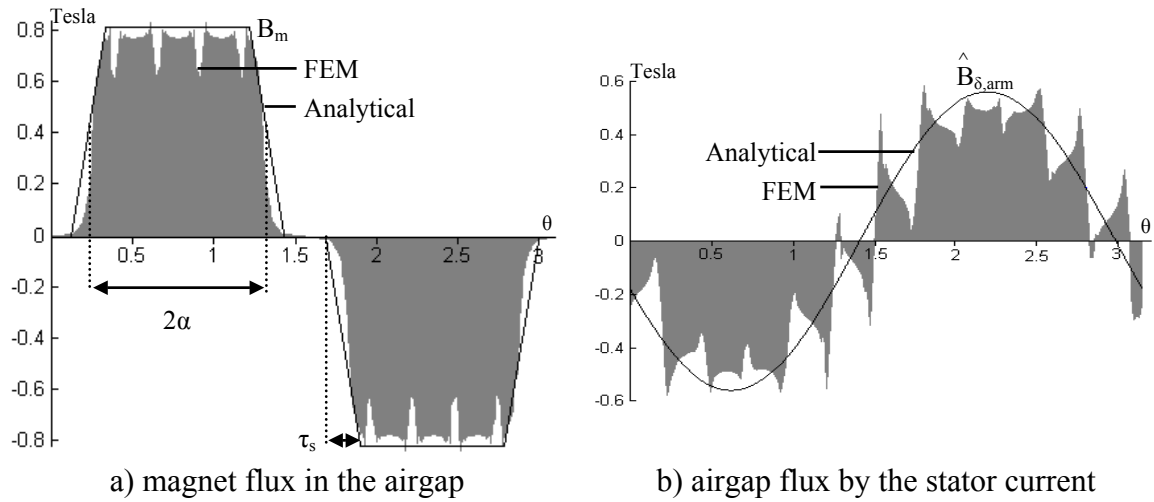


Figure 5-13 Airgap flux by the magnets and the stator current

All the airgap flux (without leakage) within a stator slot pitch τ_s ideally passes through the corresponding stator tooth. The flux density in the teeth $B_{st}(\theta)$ can be expressed by Equation 5-10, where the magnet flux and the flux by the stator current are integrated over one slot pitch.

$$B_{st}(\theta) = \frac{1}{b_{ts}} \cdot \int_{\theta}^{\theta+\tau_s} (B_m(\theta) + \hat{B}_{\delta,arm} \cdot \cos(\theta + \gamma)) \cdot d\theta \quad \text{Equation 5-10}$$

The resulting flux distribution is shown in Figure 5-14. A comparison with the simulated flux distribution from FEM shows that analytical flux levels are lower. This is due to the fact that the leakage flux is neglected. In Figure 5-14 one minor hysteresis loop is pointed out. These minor hysteresis loops contribute to the hysteresis losses. Since their detection and inclusion in the calculation is quite complex, their contribution to the losses is neglected.

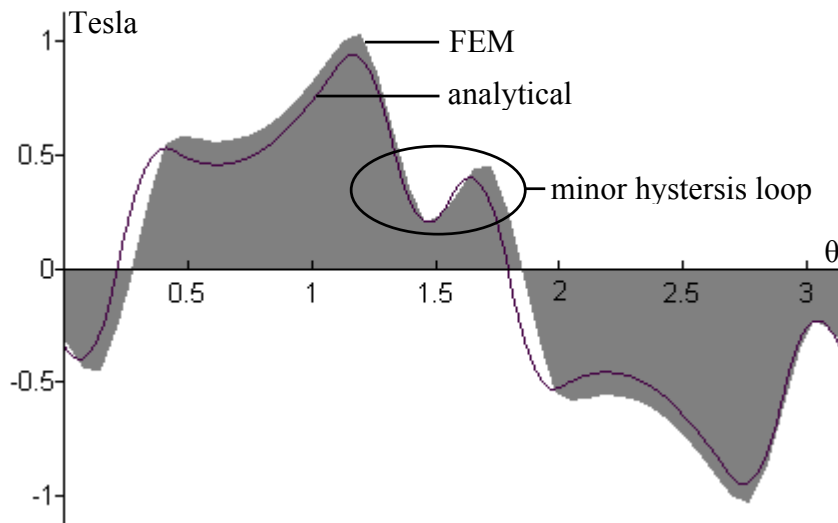


Figure 5-14 FEM and analytical flux density variation in the stator teeth

The stator teeth iron loss density in transient magnetic applications over one complete period τ can then be calculated as:

$$dp_{teeth} = \frac{1}{\tau} \cdot \int_0^{\tau} p_{iron}(\theta) \cdot d\theta = k_{hyst} \cdot \max(B_{st}(\theta))^2 \cdot f \cdot k_j + \frac{1}{\tau} \cdot \int_0^{\tau} \left[\sigma_{iron} \cdot \frac{d_{lam}^2}{12} \cdot \left(\frac{dB_{st}(\theta)}{d\theta} \right)^2 + k_{exc} \cdot \left(\frac{dB_{st}(\theta)}{d\theta} \right)^{3/2} \right] \cdot k_j \cdot d\theta \quad \text{Equation 5-11}$$

Table 5-9 shows an itemisation of the stator teeth losses. The hysteresis losses are as expected smaller than simulated with FEM. This is due to the neglect of the minor hysteresis loops and the lower levels of flux density. The analytical eddy current and excess losses are also lower than simulated. The reason is that the lower level of flux density and the strong distortions in the teeth shoes (due to the leakage flux from the current) are not included in the analytical values. The total loss in the stator teeth is 18.2% lower than the FEM losses calculated, 175.1 W.

stator teeth losses	simulated (FEM)	analytical
hysteresis loss	38.4 W	25.4 W (-33.9%)
eddy current loss	145.1 W	124.1 W (-14.4%)
excess loss	30.6 W	25.6 W (-16.2%)
total losses	214.0 W	175.1 W (-18.2%)

Table 5-9 Itemisation of the stator teeth losses

5.3.2 Stator yoke losses

The stator yoke losses are more difficult to describe than the teeth losses. The model is based on the partition of the flux distribution in radial r - and tangential θ -components. Figure 5-15 shows this partition.

Looking at the radial component of the flux distribution B_{sy_r} in Figure 5-17, the same waveform as for the flux distribution in the teeth can be noticed. The curve in Figure 5-17 is measured in the middle of the stator yoke in the prolongation of a stator tooth (corresponding to point p1 in Figure 5-16). Consequently, the iron losses for the r -component of the flux distribution in the stator yoke can be calculated from the flux distribution in the teeth $B_{st}(\theta)$. Only the amplitude has to be modified:

$$\frac{B_{sy_r}(\theta)}{|B_{sy_r}(\theta)|} = \frac{B_{st}(\theta)}{|B_{st}(\theta)|} \quad \text{Equation 5-12}$$

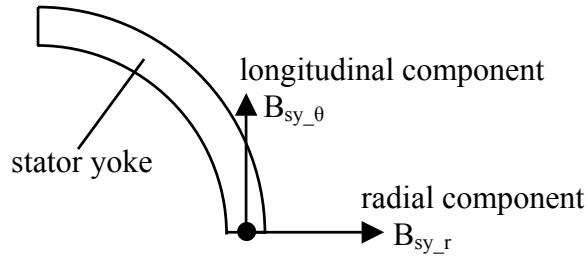


Figure 5-15 Partition of the stator yoke flux in a radial and longitudinal component

The scaling of $B_{sy_r}(\theta)$ is based on the FEM simulations. Figure 5-16 shows the flux distribution in the stator yoke and teeth in the prolongation of the stator tooth middle (corresponding to the arrow in Figure 5-16). The gradient of the flux distribution in the stator yoke can be approached as cubic resulting in the scaling factor given in Equation 5-13. More details about the calculation are given in App. B3.

$$B_{sy_r}(\theta) = \frac{B_{st}(\theta)}{\sqrt{7}}$$

Equation 5-13

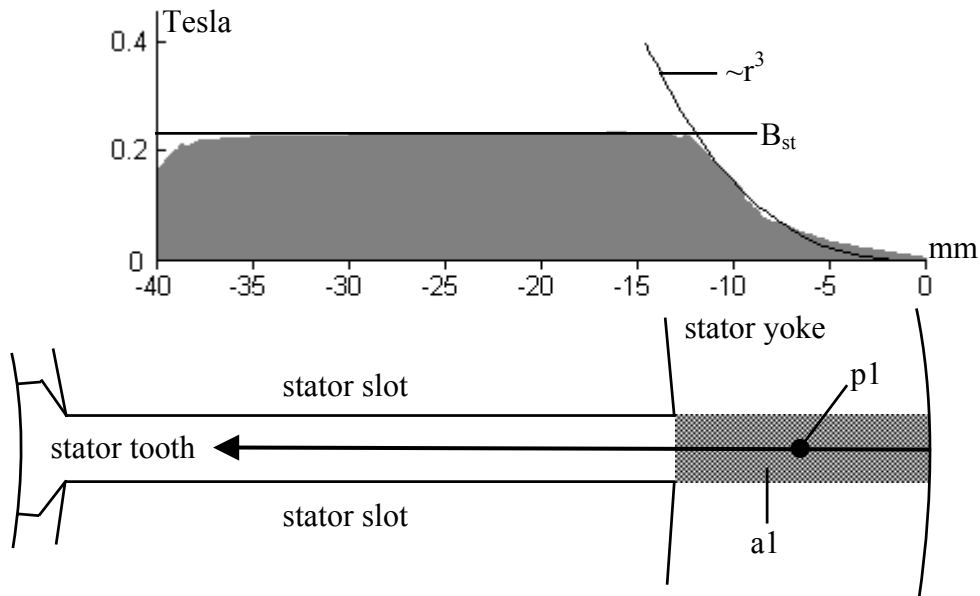


Figure 5-16 Flux distribution in the stator yoke and tooth

For the calculation of the radial component of the flux distribution in the stator yoke, it is assumed, that the r-component does only appear in the area that is in the prolongation of the stator teeth (corresponding to area a1 in Figure 5-16). Figure 5-17 shows the flux distribution in the middle of the stator yoke in the extension of a stator tooth from the FEM simulation. It can be noticed that the flux distribution is analytically overestimated; the reasons are discussed later in this chapter.

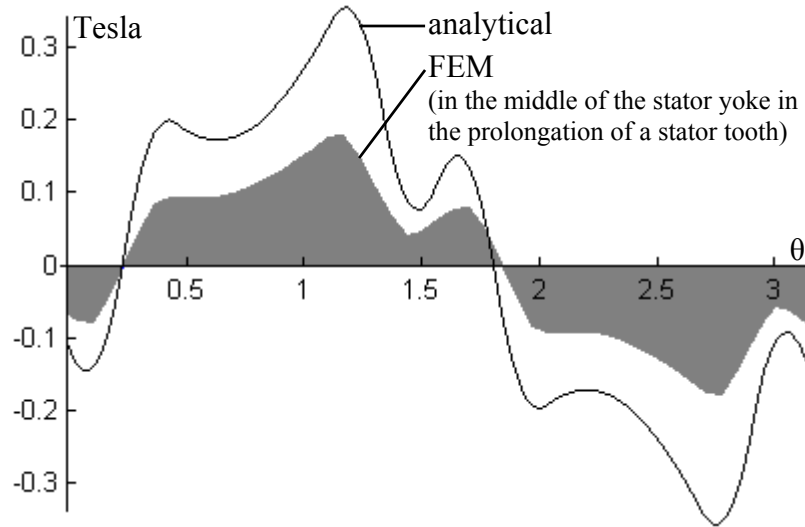


Figure 5-17 Radial component of the stator flux distribution

The tangential component of the stator flux distribution is nearly sinusoidal. The flux distribution in the middle of the stator yoke in the prolongation of a stator tooth (corresponding to point p1 in Figure 5-16) is shown in Figure 5-18.

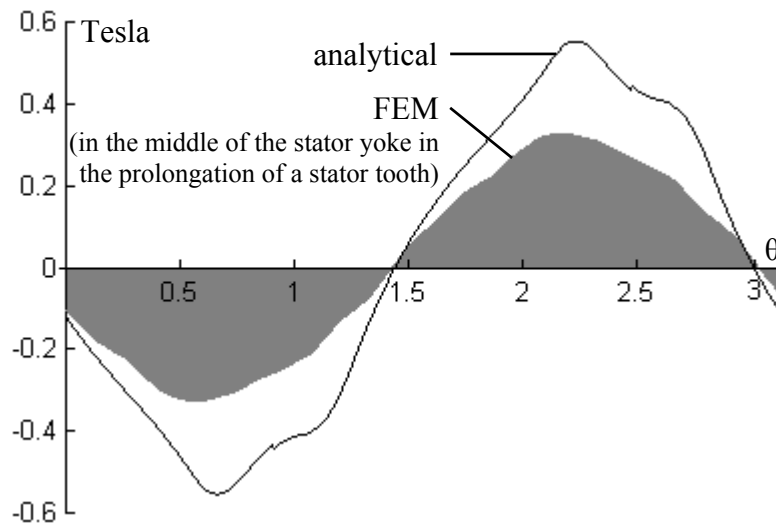


Figure 5-18 Longitudinal component of the stator flux distribution

The calculation of the tangential component of the stator flux distribution is based on the assumption, that the total airgap flux is guided through the stator teeth to the stator yoke and that it splits there and closes on both sides over the neighbouring poles. Equation 5-14 shows the expression for the calculation of the θ -component of the flux distribution in the yoke:

$$B_{sy_ \theta}(\theta) = \frac{D - \delta}{4 \cdot h_{sy}} \cdot \int_{\theta}^{2\pi/p + \theta} (B_m(\alpha) + \hat{B}_{\delta, arm} \cdot \cos(\alpha + \gamma)) \cdot d\alpha \quad \text{Equation 5-14}$$

Figure 5-18 shows the FEM and analytically calculated tangential component of the flux distribution in the stator yoke. It can be noticed again, that the flux distribution is analytically overestimated. Based on the flux distribution, the losses can be calculated in a similar way as the losses in the teeth (refer to Equation 5-11). Table 5-10 shows an itemisation of the different iron losses in the stator yoke.

stator yoke losses	simulated (FEM)	analytical
hysteresis loss	8.5 W	17.2 W (+101.4%)
eddy current loss	22.8 W	38.0 W (+67.1%)
excess loss	8.5 W	14.2 W (+67.0%)
total losses	39.8 W	69.4 W (+74.4%)

Table 5-10 Itemisation of the stator yoke losses

The analytical value of the stator yoke losses is too high due to the fact that the flux levels (of both radial and tangential component) are overestimated. The reason is that the leakage flux through the tooth shoe and the stator slot is not considered. Thus the flux density in the yoke from the current alone is much too low (the analytical value of $B_{sy_ \theta}$ is 0.67 T, compared to a value of 0.96 T in FEM). For field-weakening operation, the flux from the stator current opposes the magnet flux. When this opposing flux is calculated too small, the resulting flux is too high and therefore the losses are overestimated.

5.3.3 Leakage model

To include the leakage flux created by the currents through the shoes and the stator slots, correction factors are introduced in the calculation of the flux densities in the airgap, yoke and teeth. The correction factors are obtained from an equivalent reluctance model of half a pole magnetized by the current in one slot (see Figure 5-19).

The flux created by the current on the chosen slot goes through the first tooth and a part of that flux is leaking through the slot and the shoe. The other part of the flux goes through the other teeth under the half pole and does not leak (R_{t2} and R_{g2}).

Due to the leakages, the flux created by the currents in the air gap is lower than previously calculated. Equation 5-10 is corrected by multiplying $\hat{B}_{\delta, arm}$ by k_{gap} , which is defined by:

$$k_{gap} = \frac{\Phi_{g2} + \Phi_{g1}}{\Phi_{gref}}, \text{ with } \Phi_{gref} = \frac{nI}{R_{g1} + R_{g2}} \quad \text{Equation 5-15}$$

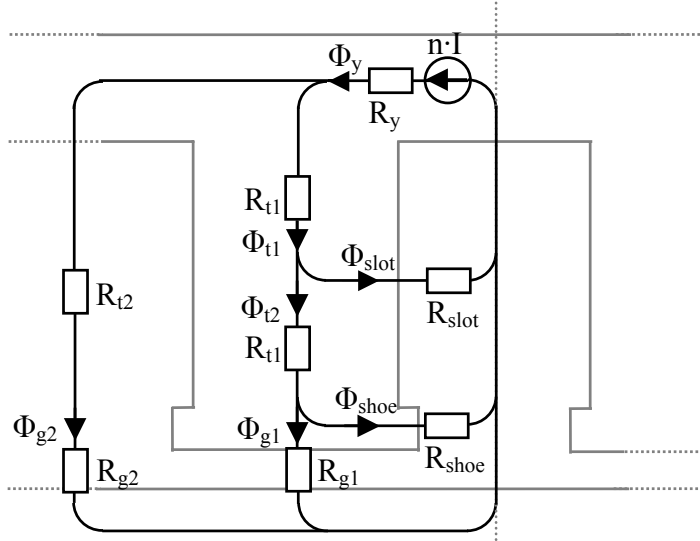


Figure 5-19 Equivalent reluctance model

Furthermore, a mean value B_{leak} is added to the flux density in the teeth to take into account the leakage flux Φ_{shoe} and Φ_{slot} . B_{leak} is obtained by integrating the airgap flux density created by the current shifted by 90° with a corrected value of $\hat{B}_{\delta,arm}$. Equation 5-10 becomes

$$B_{st}(\theta) = \frac{1}{b_{ts}} \cdot \int_{\theta}^{\theta+\tau_s} \left(B_m(\theta) + \hat{B}_{\delta,arm} \cdot k_{gap} \cdot \cos(\theta + \gamma) + \hat{B}_{leak} \cdot \cos\left(\theta + \gamma - \frac{\pi}{2}\right) \right) \cdot d\theta$$

Equation 5-16

with $\hat{B}_{leak} = k_{teeth} \cdot \hat{B}_{\delta,arm} \cdot k_{gap}/q_s$ and $k_{teeth} = \frac{\Phi_{t2} + \Phi_{t1}}{\Phi_{g1}}$.

Figure 5-20 shows the obtained flux density in the middle of a tooth at 178 Hz.

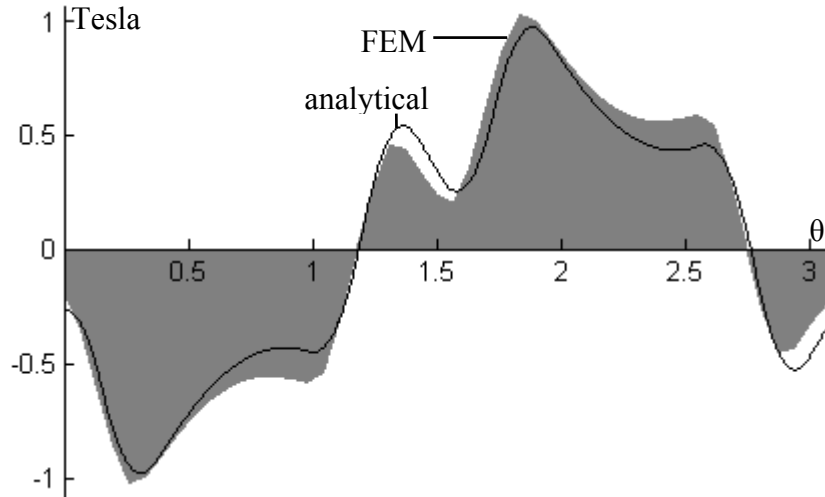


Figure 5-20 Flux density in the stator teeth

The iron losses in the shoes are now included in the model. It is assumed that the flux density in the shoe is a combination of the flux density in the air gap created by the magnet and the one created by the current corrected by the factor k_{shoe} :

$$B_{shoe}(\theta) = \sqrt{(\hat{B}_{\delta,arm}(\theta) \cdot k_{shoe})^2 + B_m^2(\theta)} \quad \text{Equation 5-17}$$

$$\text{with } k_{shoe} = 2 \cdot \frac{\Phi_{shoe}}{\Phi_{t2} + \Phi_{t1}} \cdot \frac{b_{ts}}{h_{sw}}$$

The radial component of the flux density distribution in the yoke B_{sy_r} is not corrected because it is derived from B_{st} that is already corrected. For B_{sy_θ} , Equation 5-14 is corrected by multiplying $\hat{B}_{\delta,arm}$ by k_{yoke} . k_{yoke} is defined as:

$$k_{yoke} = \frac{\Phi_y}{\Phi_{gref}} \quad \text{Equation 5-18}$$

Figure 5-21 shows the obtained tangential component of the flux density in the middle of the stator yoke at 178 Hz.

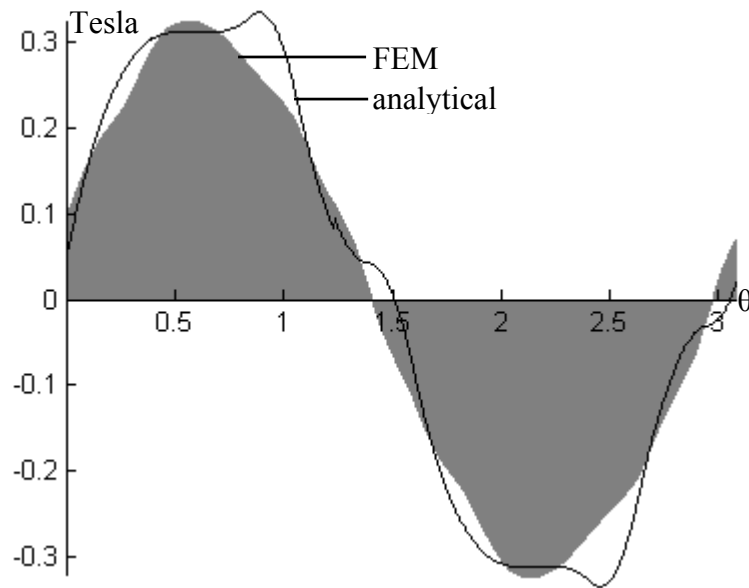


Figure 5-21 Tangential component of the flux density in the stator yoke

Table 5-11 compares the iron losses at 178 Hz with and without the leakage model derived in this section. It can be noticed, that the prediction of the iron losses in the different parts of the machine is more accurate with the use of the leakage model.

	teeth	shoe	teeth & shoe	yoke	total
no leakage*	175.1 W	-	-	69.4 W	244.5 W
with leakage*	185.6 W	23 W	208.7 W	39.4 W	248 W
FEM	-	-	214 W	39.8 W	253.8 W

* "no leakage" corresponds to the loss model without including the leakage model from section 5.3.3. "with leakage" includes the leakage model.

Table 5-11 Iron losses at 178 Hz with and without inclusion of the leakage model

Table 5-12 compares the analytical iron losses including the leakage model with the simulated FEM iron losses. The iron loss model gives a total value of the stator iron losses that is less than 17 % different from the FEM results.

frequency	50 Hz	114 Hz	178 Hz	242 Hz	306 Hz
with leakage model	135 W	159 W	248 W	382 W	560 W
FEM	116 W	166.5 W	258.5 W	363.5 W	511 W

Table 5-12 Comparison of the FEM and analytical iron losses at different frequencies

Table 5-13 compares the losses for the compact motor design from section 4.2.3. There is a problem, that the rated torque in the FEM simulation is only 50 Nm. The correction of the torque taking the leakage into account (refer to Equation 5-5) is not sufficient. To compensate that drop in the torque, the stator current for the analytical model and the FEM simulation was increased by the factor 6/5. The new torque in FEM is 57.5 Nm.

It can be seen from Table 5-13, that the iron loss prediction works quite good for higher frequencies. At lower frequencies around the base speed, there is an overestimation of the iron losses, especially in the stator yoke.

Frequency f		teeth	shoe	teeth & shoe	yoke	total
50 Hz	FEM	-	-	42.5 W	59.5 W	102 W
	analytic	41 W	2 W	43 W	84 W	127 W
135 Hz	FEM	-	-	120 W	47 W	167 W
	analytic	74 W	18 W	92 W	63.5 W	155.5 W
219 Hz	FEM	-	-	220.5	52 W	272.5 W
	analytic	144.5 W	54 W	198.5 W	58.5 W	257 W
304 Hz	FEM	-	-	369.5 W	64.5 W	434 W
	analytic	242.5 W	116 W	358.5 W	61 W	419.5 W

Table 5-13 FEM and analytical iron losses for the compact motor design

Figure 5-22 shows a comparison of the different analytical iron loss models to the FEM results. A better iron losses model was obtained with the inclusion of the stator leakage. It should be good enough to compare the performances of different motors but the exact values of the stator iron losses should still be checked with FEM once a geometry is chosen.

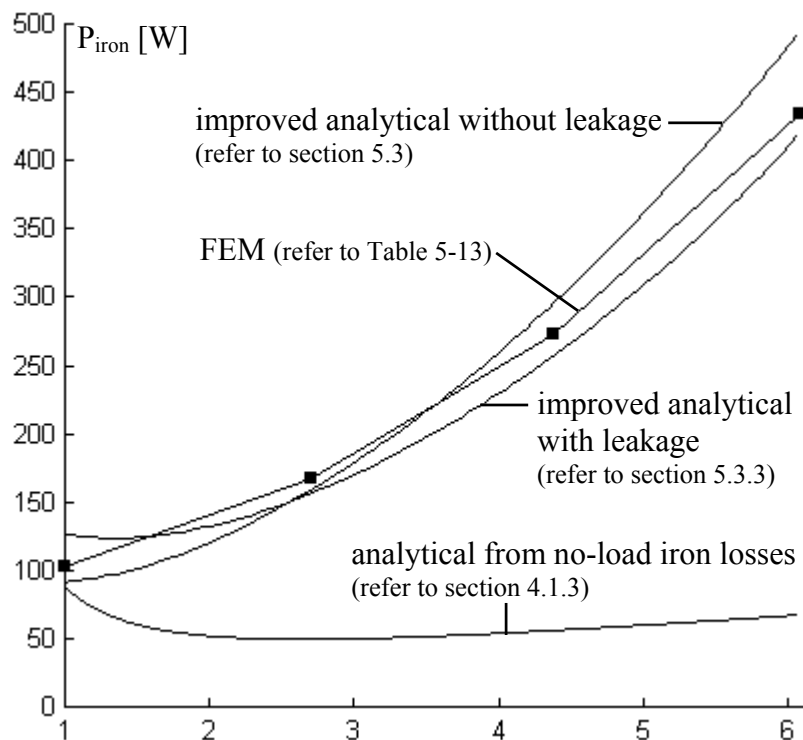


Figure 5-22 Comparison of different analytical iron loss models for the compact motor design

6 Conclusions and future work

Conclusions

In this master thesis, an analytical design program for SMPM-motors was developed. The model includes tools for the prediction of the field-weakening performance. The maximum field-weakening speed and the constant power speed range (CPSR) including the iron losses are calculated. The iron loss model is based on the prediction of the flux distribution in different parts of the stator. This is done with the help of an equivalent reluctance model. The correctness of the analytical design program is proved with FEM simulations.

The model does not include the effects of saturation and stray losses. To improve the analytical prediction of the SMPM performance, the saturation and the stray losses should be included. In the same way, the minor hysteresis loops that are not considered in the calculation of the hysteresis losses should be included. In addition, the correction factor for the torque introduced in Equation 5-5 to take into account the armature leakage flux should be improved. A possibility is to use the equivalent reluctance model introduced in chapter 5.3. The approach that only considers the shoe leakage inductance is not sufficient.

The design procedure was used to do a short parametric study so that the influence of several parameters could be pointed out.

It is shown in section 4.2, that the stator of the induction motor can be used for a SMPM motor. A 6-pole design looks promising. For a 4-pole design, the stator yoke is too thin and gets saturated. It is also shown, that a compact (smaller outer dimensions than the induction motor) 4-pole design is possible with better efficiency compared to the induction motor.

Future work

Stray losses can severely affect the field-weakening performances so a stray losses model should be derived to complete the prediction of the losses.

A thermal model should be implemented to complete the analytical design program. A thermal model would help to reach an optimal design as the current density would not be limited arbitrarily anymore.

Once the analytical model is all right, an optimal design for the application in the forklift should be derived.

A prototype should be built to prove the analytical model and the predicted performances.

References

- [1] *Soong, W.L. and Miller, T.J.E.*: Field-weakening performance of brushless synchronous AC motor drives. IEE Proc.-Electr. Power Applications, Vol. 141, No. 6, November 1994.
- [2] *Hendershot, J.R. and Miller T.J.E.*: Design of brushless permanent-magnet motors. Magna Physics Publishing and Oxford Science Publications, 1994.
- [3] *Schiffertl, R.F. and Lipo, T.A.*: Power capability of salient pole permanent magnet synchronous motor in variable speed drive applications. IEEE Trans., 1990.
- [4] *Sebastian, T. and Slemon, G.R.*: Operating limits of inverter-driven permanent magnet motor drives. IEEE Trans., 1987.
- [5] *Chin, R.*: Literature study on PM machines: Field-weakening operation & loss prediction. Royal Institute of Technology, Sweden, 2001.
- [6] *Bianchi, N. and Bolognani, S.*: Innovative design and optimisation of electrical machines, Part: Optimal motor design for flux-weakening applications. Post-graduate seminar, Helsinki University of Technology, 2001.
- [7] *Hellsing, J.*: Design and optimization of a permanent magnet motor for a hybrid electric vehicle. Lic. Tech. Thesis, Technical Report No. 282L, Chalmers University of Technology, Sweden, 1998.
- [8] *Sadarangani, C.*: Electrical Machines - Design and analysis of induction and permanent magnet motors. Royal Institute of Technology, Sweden, 2000.
- [9] *Mi, C., Slemon, G.R. and Bonert, R.*: Modeling of iron losses of surface-mounted permanent magnet synchronous motors. IEEE, 2001.
- [10] *Slemon, G.R. and Liu, X.*: Core losses in permanent magnet motors. IEEE Transaction on Magnetics, Vol. 26, No. 5, pp. 1653 - 1655, 1990.
- [11] *Wijenayake, A.H. and Schmidt, P.B.*: Modeling and analysis of permanent magnet synchronous motor by taking saturation and core loss into account. IEEE, 1997.
- [12] Flux2D (Version 7.5) Tutorial: Brushless permanent magnet motor. CEDRAT, 2001.
- [13] *Morimoto, S., Takeda, Y., Hirasa, T. and Taniguchi, K.*: Expansion of operating limits for permanent magnet motor by current vector control considering inverter capacity. IEEE Trans. IAS-26, pp. 886 - 871, 1990.
- [14] *Arshad, W.*: Application of SMC iron powder materials in electrical machines. M.Sc thesis, KTH, 1998.
- [15] *Libert, F.*: Theoretical design of a 75 kW 4-pole line-start permanent magnet synchronous motor. M. Sc thesis (EX-EME-0201), KTH, 2002.
- [16] *Oberretl, K.*: Iron losses, flux pulsation and magnetic slot wedges in squirrel cage motors. Electrical Engineering, vol. 82, no. 6, p. 301-311, Springer Verlag, Germany, 2001.

List of Symbols and Abbreviations

List of Abbreviations

AC	alternating current
CPSR	constant power speed range
DC	direct current
FEM	finite element method
IPM	interior PM-motor
PM	permanent magnet
PMD	Permanent Magnet Drives Program
SMPM	surface-mounted PM-motor
Synchrel	synchronous reluctance motor

List of Symbols

subscript _n indicates normalised parameters
 subscript _b indicates base (or nominal/rated) parameters
 ^ indicates the peak value of a sinusoidal parameter

A_{cond}	copper area of one conductor	[m ²]
A_{cu}	copper area per slot	[m ²]
A_{sl}	stator slot area	[m ²]
B_{D}	demagnetisation flux density of the magnet	[T]
B_{m}	maximum value of flux density in the airgap above the magnets	[T]
B_{r}	remanence flux density of the magnet at operating temperature	[T]
B_{ry}	maximum flux density in the rotor yoke	[T]
b_{ss1}	inner stator slot width	[m]
b_{ss2}	outer stator slot width	[m]
B_{st}	maximum flux density in the stator teeth	[T]
B_{sy}	maximum flux density in the stator yoke	[T]
b_{ts}	stator tooth width	[m]
\hat{B}_{δ}	fundamental airgap flux density	[T]
c	parallel coupling factor	
cov	magnet coverage	
D	inner stator diameter	[m]
D_{i}	shaft diameter	[m]
d_{lam}	lamination sheet thickness	[m]
D_{rc}	rotor core diameter	[m]
D_{y}	outer stator diameter	[m]
E	fundamental induced voltage (back EMF)	[V]
f	electrical frequency	[Hz]
f_{s}	fill factor of the stator winding	
h_{m}	magnet height (or thickness)	[m]
h_{ry}	height of the rotor yoke	[m]

List of Symbols and Abbreviations

h_{ss}	height of the stator slot	[m]
h_{sw}	height of the stator wedge	[m]
h_{sy}	height of the stator yoke	[m]
I	terminal current	[A]
I_d	d-axis component of the terminal current I	[A]
I_q	q-axis component of the terminal current I	[A]
J	current density	[A/mm ²]
k_c	correction factor taking the circumferential flux component into account	
k_{carter}	Carter factor	
k_{coil}	empirical constant taking the end windings arrangement into account	
k_{eddy}	eddy current loss constant	[W·s ² /T ² /m ³]
k_{exc}	excess loss constant	[W·(s/T) ^{3/2} /m ³]
k_{hyst}	hysteresis current constant	[W·s/T ² /m ³]
k_j	stator iron stacking factor due to the lamination	
k_{leak}	empirical constant for the rotor flux leakage	
k_{open}	ratio of stator opening width to stator slot width (see Figure 4-2)	
k_q	correction factor taking motor geometry into account	
k_{w1}	winding factor for the first harmonic	
l	active length of the lamination	[m]
L_d	d-axis inductance	[H]
L_{leak}	stator leakage inductance	[H]
L_m	magnetising inductance	[H]
L_q	q-axis inductance	[H]
m	number of phases	
N	number of turns per phase	
n_s	number of conductors per stator slot	
p	number of poles	
P_{cu}	copper losses	[W]
p_{eddy}	eddy current loss density	[W/m ³]
p_{hyst}	hysteresis current loss density	[W/m ³]
p_{iron}	iron loss density	[W/m ³]
P_{iron}	total iron (core) losses	[W]
P_{out}	output power	[W]
q	number of stator slots per pole per phase	
Q_s	number of stator slots	
R_{cu}	copper loss resistance	[Ω]
R_{eddy}	eddy current loss resistance	[Ω]
R_{hyst}	hysteresis loss resistance	[Ω]
R_{iron}	iron loss resistance	[Ω]
S_1	sinusoidal stator current loading	[A/m]
T	torque	[Nm]
U	terminal voltage (equal to inverter output voltage)	[V]
U_d	d-axis component of the terminal voltage U	[V]
U_{L-L}	rms-value of the line-to-line inverter output voltage	[V]
U_q	q-axis component of the terminal voltage U	[V]
w_m	circumferential width of the magnet	[m]
V_t	volume of the stator teeth	[m ³]

List of Symbols and Abbreviations

V_y	volume of the stator yoke	[m ³]
α	half pole angle in electrical degrees	[rad]
2α	pole angle	[rad]
β	electrical angle between the current and the magnet flux vector	[rad]
β_{St}	Steinmetz constant	
γ	current angle between induced voltage E and terminal current I	[rad]
δ	airgap length	[m]
δ_e	equivalent airgap length (including the effect of stator slotting)	[m]
η	efficiency	
μ_0	magnetic field constant ($4\pi \cdot 10^{-7}$)	[Vs/Am]
μ_r	relative permeability of the magnet	
ξ	saliency ratio	
ρ_{cu}	copper resistivity ($17.2e-9 \Omega m$ @ $20^\circ C$)	[Ωm]
ρ_{iron}	iron lamination resistivity	[Ωm]
σ_{iron}	iron lamination conductivity	[$\Omega^{-1} m^{-1}$]
τ_s	stator slot pitch	[m]
$\cos(\varphi)$	power factor	
Φ_m	fundamental magnetic flux	[Wb]
Φ_{mp}	magnetic flux per pole	[Wb]
Φ_{sy}	maximum flux in the stator yoke	[Wb]
Ψ_m	magnet flux linkage	[Wb]
ω	electrical angular frequency	[Hz]
ω_{el}	electrical angular velocity	[Hz]
ω_{mech}	mechanical angular velocity	[Hz]

App. A Powder materials and concentrated windings

Interests in finding suitable alternatives to replace steel laminations in electrical machines have grown recently due to the emerging iron powder materials. Soft-magnetic composites (SMC) offer superiority in manufacturing techniques, allow 3D design freedoms due to their isotropic nature and exhibit negligible eddy current losses at lower frequencies due to the insulation of each individual iron particle. On the other hand, lower achievable induction levels and poorer relative permeability as compared to steel laminations are expected.

Waqas Arshad has done some credible investigations on the application of SMC in electrical machines [14]. He concluded that a PM powder machine has a performance only slightly worse than that of a laminated PM machine for the same geometrical dimensions. One of his interesting findings was that iron losses in powder material are larger than in steel laminations at lower frequencies but smaller at high frequencies. Consequently, the use of powder materials should be taken into account especially when designing high-frequency applications.

The use of windings concentrated around the teeth offer obvious advantages for electrical machines with radial airgap. The volume of copper used in the end-windings can be significantly reduced, having the effect of lessening the copper losses in the windings. Generally, a concentrated winding is effective with regard to downsizing the motor.

According to the literature studies of Robert Chin [5], the main disadvantage of concentrated winding is that the EMF waveform is more distorted and contains significant higher harmonics. This leads to additional iron losses causing an inferior performance¹⁶ compared to machines with distributed windings.

The use of soft magnetic composites with concentrated windings could simplify the production process and shows great promise for high-speed applications.

¹⁶ lower maximum torque, shorter constant power speed region (CPSR)

App. B Parameter calculations

App. B1 Calculation of the magnetising inductances

For a non-salient pole SMPM, the d- and q-axis inductances should be the same. Due to the fact of the permanent magnet permeability, L_d may slightly differ from L_q . In my work I did not take this difference into account and was assuming non-salient conditions with L_q having the same value as L_d . Subsequently, the calculation of the d- and q-axis inductances is affiliated.

The d-axis inductance L_d can be calculated ignoring iron saturation by

$$L_d = \frac{\hat{\Psi}_{d,armature}}{\hat{I}_d} = \frac{N \cdot \hat{\Phi}_{d,armature}}{\hat{I}_d}$$

with

$$\hat{\Phi}_{d,armature} = \hat{B}_{d,armature} \cdot \frac{\pi \cdot (D - \delta) \cdot l}{p} \cdot \frac{2}{\pi}$$

and

$$\hat{B}_{d,armature} = \mu_0 \cdot \hat{H}_{d,armature} = \mu_0 \cdot \frac{\frac{4}{\pi} \cdot \frac{3}{2} \cdot \hat{I}_d \cdot q \cdot n_s \cdot k_{w1}}{\delta_e + \frac{l_m}{\mu_r}}$$

The result for the d-axis inductance L_d is then:

$$L_d = \frac{3}{\pi} \cdot (q \cdot n_s \cdot k_{w1})^2 \cdot \frac{\mu_0}{\delta_e + \frac{l_m}{\mu_r}} \cdot (D - \delta) \cdot l$$

The q-axis inductance L_q can be calculated in the same way resulting in

$$L_q = \frac{3}{\pi} \cdot (q \cdot n_s \cdot k_{w1})^2 \cdot \frac{\mu_0}{\delta_e + \frac{l_m}{\mu_r}} \cdot (D - \delta) \cdot l$$

App. B2 Calculation of the stator leakage inductance

The stator slot leakage inductance is caused by leakage flux crossing a slot. The magnetic field strength in the stator can be approximately calculated by the use of Ampere's circuit law. For the calculation of the stator leakage inductance, the following simplifications are supposed: The leakage flux is assumed to cross the slot width in straight lines perpendicular to the slot sides. Skin effect is neglected and the permeability of iron is assumed to be infinite.

For the calculation of the stator leakage inductance, we consider a rectangular slot geometry as shown in Figure B-1 below. It is quite obvious that the field strength increases linearly with the slot height. The field strength at any stator height, especially at the slot opening can be calculated using the Kirchoff's voltage law. According to it, the algebraic sum of ampere-turns around a closed path in a magnetic circuit is equal to the algebraic sum of the products of the reluctances and fluxes. The algebraic sum of ampere-turns of a path around the slot and passing the slot opening in the upper part (with the width $b_{ss1} \cdot k_{open}$) can be calculated by integration of the magnetic field strength H_{max} :

$$n_s \cdot I_{cond} = \oint H \cdot db = H_{max} \cdot b_{ss1} \cdot k_{open}$$

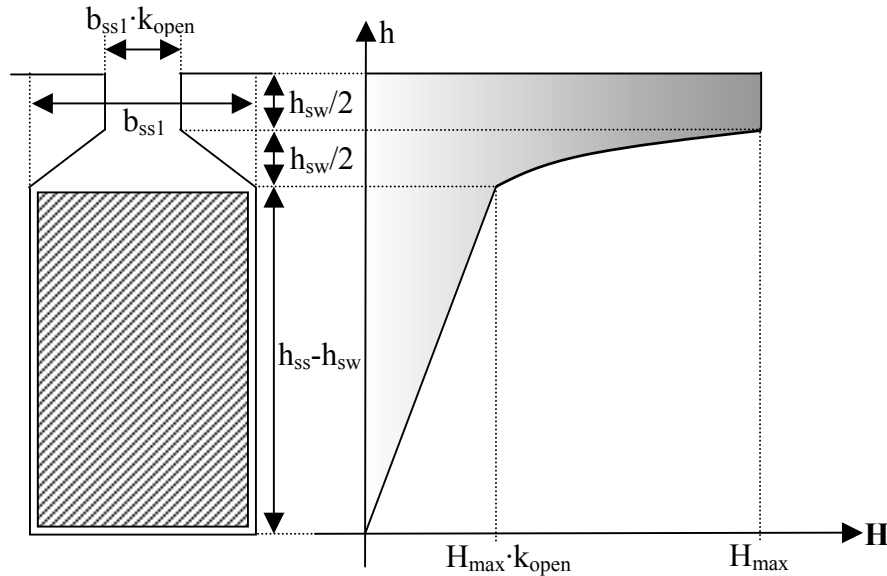


Figure B-1 Distribution of the leakage field in a slot

The magnetic field energy of the slot opening W_{so} can be written as follows:

$$\begin{aligned}
 W_{so} &= \frac{1}{2} \int_V H \cdot B \cdot dV = \frac{1}{2} \int_V \mu_0 \cdot H^2 \cdot dV = \\
 &= \frac{\mu_0}{2} \cdot l \cdot \left(\int_0^{h_{sw}/2} b_{ss1} \cdot \left(k_{open} + \frac{2h}{h_{sw}} - k_{open} \cdot \frac{2h}{h_{sw}} \right) \cdot \left(\frac{H_{max} \cdot k_{open}}{k_{open} + \frac{2h}{h_{sw}} - k_{open} \cdot \frac{2h}{h_{sw}}} \right)^2 dh + H_{max}^2 \cdot \frac{h_{sw}}{2} \cdot b_{ss1} \cdot k_{open} \right) = \\
 &= \frac{\mu_0}{2} \cdot l \cdot H_{max}^2 \cdot b_{ss1} \cdot \frac{h_{sw}}{2} \cdot \left(k_{open} + \frac{k_{open}^2}{1 - k_{open}} \cdot \left(\ln \left(\frac{h_{sw}}{2 - 2k_{open}} \right) - \ln \left(\frac{h_{sw} \cdot k_{open}}{2 - 2k_{open}} \right) \right) \right) = \frac{1}{2} \cdot \mu_0 \cdot n_s^2 \cdot I_{cond}^2 \cdot l \cdot \lambda_1
 \end{aligned}$$

where the ratio λ_1 is called the specific permeance coefficient of the slot opening. It can be expressed for the slot opening arrangement in Figure B-1 in the following way

$$\lambda_1 = \frac{h_{sw}}{2 \cdot b_{ss1} \cdot k_{open}} + \frac{h_{sw}}{2 \cdot b_{ss1} \cdot (1 - k_{open})} \cdot \left(\ln \left(\frac{h_{sw}}{2 - 2k_{open}} \right) - \ln \left(\frac{h_{sw} \cdot k_{open}}{2 - 2k_{open}} \right) \right)$$

The magnetic field energy of the slot W_s can be written as follows:

$$W_s = \frac{1}{2} \cdot L_{leak} \cdot I^2$$

By setting the equation for the magnetic field energy of a slot (W_s) equal to the equation for the magnetic field energy of the slot opening (W_{so}), the resultant reactance for a slot can be found. The stator slot leakage inductance per phase is then given by the multiplication with the number of stator slots per phase.

$$L_{leak} = p \cdot q \cdot n_s^2 \cdot l \cdot \mu_0 \cdot \lambda_1$$

App. B3 Calculation of the scaling factor for the radial yoke flux component

In this appendix, the calculation of the scaling factor for the radial yoke flux component B_{sy_r} is shown. Figure B2 shows the dimensions and the flux distribution in the stator yoke (compare to chapter 5.3.2 and Figure 5-16).

$$B_{sy_r}(r) = B_{st} \cdot \frac{r^3}{h_{sy}^3}$$

$$\begin{aligned} \langle B_{RMS} \rangle_{sy_r} &= \sqrt{\frac{1}{h_{sy}} \cdot \int_0^{h_{sy}} B_{sy_r}^2(r) \cdot dr} = \frac{1}{\sqrt{h_{sy}}} \cdot \sqrt{\int_0^{h_{sy}} \frac{B_{st}^2 \cdot r^6}{h_{sy}^6} \cdot dr} \\ &= \frac{B_{st}}{\sqrt{h_{sy}}} \cdot \sqrt{\left[\frac{r^7}{7 \cdot h_{sy}^6} \right]_0^{h_{sy}}} = \frac{B_{st}}{\sqrt{h_{sy}}} \cdot \frac{h_{sy}^{7/2}}{\sqrt{7} \cdot h_{sy}^3} = \frac{B_{st}}{\sqrt{7}} \end{aligned}$$

$$\langle B_{RMS} \rangle_{sy_r} = \frac{B_{st}}{\sqrt{7}}$$

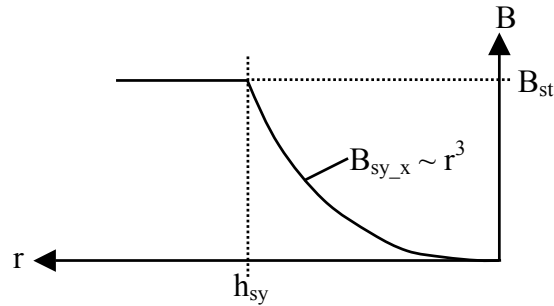


Figure B-2 Distribution of the leakage field in a slot

App. C Park transformation

The Park transformation is used to transform three-phase systems into two-axis models. Since different scaling approaches can be found that often cause confusion, the Park transformation is summarized in this appendix.

Assuming a symmetric three-phase system (phases a, b and c), a transformation from this system to a two-axis model (axis d and q) is possible. For synchronous motors, especially with permanent magnets, a rotor-oriented coordinate system is more convenient. In the dq-system, the d-axis is along the magnetisation of the rotor while the q-axis lies electrically perpendicular ahead in the direction of positive rotation [15].

The transformation of the three-phase voltage to the dq-quantities is defined by the following equations:

$$U_d = \frac{2}{3} \cdot K \cdot (U_a \cdot \sin(\omega_{el}t) + U_b \cdot \sin(\omega_{el}t - 2\pi/3) + U_c \cdot \sin(\omega_{el}t + 2\pi/3))$$
$$U_q = \frac{2}{3} \cdot K \cdot (U_a \cdot \cos(\omega_{el}t) + U_b \cdot \cos(\omega_{el}t - 2\pi/3) + U_c \cdot \cos(\omega_{el}t + 2\pi/3))$$

The inverse transformation is then

$$U_a = \frac{1}{K} \cdot (U_d \cdot \sin(\omega_{el}t) + U_q \cdot \cos(\omega_{el}t))$$
$$U_b = \frac{1}{K} \cdot (U_d \cdot \sin(\omega_{el}t - 2\pi/3) + U_q \cdot \cos(\omega_{el}t - 2\pi/3))$$
$$U_c = \frac{1}{K} \cdot (U_d \cdot \sin(\omega_{el}t + 2\pi/3) + U_q \cdot \cos(\omega_{el}t + 2\pi/3))$$

These transformations are also valid for the phase current and linkage flux. In synchronous steady-state operation, the dq-quantities are constant. The three-phase system is thereby transformed into a system with two decoupled axes (if the cross-coupling due to saturation is neglected). The scaling constant K can be chosen arbitrary. Depending on the application, one choice may be more convenient than another. Three values are of special interest:

$$K=1: \quad \text{peak-value scaling}$$
$$K=\frac{1}{\sqrt{2}}: \quad \text{rms-value scaling}$$
$$K=\sqrt{\frac{3}{2}}: \quad \text{power invariant scaling}$$

In this work, $K=1$ was used. That means that the peak-values of the voltage and the current remain the same, in return the power in the dq-system is only one third of the power in the three-phase system ($P_{dq}=P_{abc}/3$).

App. D Magnet shape and magnetisation

Regarding the iron losses, it is desirable to have a sinusoidal magnetic field in the airgap. Using radially magnetised magnets of constant height (see Figure D-1a) produces a trapezoidal magnetic field shape. The steep edges cause high eddy current losses (compare to chapter 4.1.3). This appendix shows some alternatives and their advantages and problems.

App. D is based on knowledge gained during the seminar "Magnetisation of Permanent Magnets for Electrical Machines" hold on 22. November 2001 at KTH. The focus of this seminar was on the presentation of the different types of permanent magnets and their properties as well as on the theory of magnetisation.



Figure D-1 Magnet shape and magnetisation

Figure D-1 shows the three different magnet shapes and magnetisations that are further studied. On the left side, the radially magnetised magnets have a constant height h_m . In the middle, the magnet shape is adjusted to give a more sinusoidal flux distribution in the airgap. A common solution is to cut the edges of the magnets to soften the flux distribution. In return, there is a higher risk of demagnetisation at the thin parts of the magnets (the magnet height h_m should be bigger than 2-2.5 mm for manufacturing).

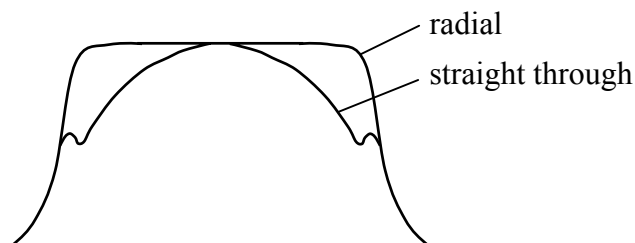


Figure D-2 Airgap flux for different magnetisations

The straight through magnetisation shown in Figure D-1c is another possibility to get a more sinusoidal field. Figure D-2 shows the airgap flux distribution for radial and straight through magnetisation. The biggest disadvantage of the straight through magnetisation is the lower peak value of the first harmonic of the flux density (compared to radial magnetisation) that must be compensated with more magnet material.

When designing a PM-machine, the different possibilities of magnet shapes and magnetisation should be considered and discussed with the supplier of the magnets at the beginning of the development project.